Fermilab

FERMILAB-THESIS-1994-50

A STUDY OF CHARMED MESON DECAYS USING THE 500 GeV π^- BEAM AT THE FERMI NATIONAL ACCELERATOR LABORATORY

A Dissertation submitted to the

Division of Research and Advanced Studies
of the University of Cincinnati

in partial fulfillment of the
requirements for the degree of

DOCTOR OF PHILOSOPHY

in the Department of Physics
of the College of Arts and Sciences

May, 1994

by

Attanagoda K. S. Santha

B.Sc.(Hon), University of Colombo, Sri Lanka, 1984
M.Sc., University of Cincinnati, 1989

Committee Chair: Michael D. Sokoloff

Abstract

A Study of Charmed Meson Decays Using the 500 GeV π^- Beam
at The Fermi National Accelerator Laboratory

by

Attanagoda K. S. Santha

Using 30% of the data from the Fermilab experiment E791, I have studied the substructure of the singly Cabibbo suppressed decays $D^0 \to K^0_S K^{\pm}\pi^{\mp}$ and have made comparisons with the Cabibbo allowed decay $D^0 \to K^0_S \pi^+\pi^-$. I see a clear $K^0_S K\pi$ signal from the resonant decay $D^0 \to K^{*+}K^-$ but no signals are observed in the K^+K^{*-}, $K^0\overline{K}^{*0}$, $\overline{K}^0 K^{*0}$ or in non-resonant modes. I report an absolute branching ratio of $(1.1 \pm 0.2 \pm 0.2)\%$ for the resonant decay $D^0 \to K^{*+}K^-$. 90% confidence level upper limits are reported for the other resonant and non-resonant decays contributing to the final states $K^0_S K^{\pm}\pi^{\mp}$.

Dedication

To the loved ones who changed my life for ever

My father, A. K. Suraweera, who did not get much to see of his son; who would have been the happiest man on earth, had he lived today. My mother, M. Katugampola, for her courage and determination; especially for raising me single handedly since my farther passed away twenty three years ago. My sister, A. K. Deepthi Indrika, for being there in happiness and sorrow. My loving wife, Kumudini, for all her love and support, without whom I could not have achieved the things I enjoy today. My daughter, Saritha for all the joy she brings to our lives.

Acknowledgements

It was a wonderful experience to read for a Ph.D. in experimental particle physics. I am very thankful to the Department of Physics at the University of Cincinnati for giving me an opportunity to pursue graduate studies in physics. My special thanks to Mike Sokoloff for supervising me through the years leading to my Ph.D.; for his professional relationship with me as my thesis advisor; for understanding my needs and being there when I needed him. I thank Rohana Wijewardhana for his friendship, encouragements, and support, which made my stay at Cincinnati more enjoyable. To Ian Stockdale, a former member of my thesis committee: I thank you for making me the computer programmer I am today. I thank Brian Meadows for his valuable discussions on various issues and the support he has given me. I thank Randy Johnson for his professional discussions and correcting numerous mistakes in this thesis. I thank Robert Endrof for serving in my thesis committee. I would like to thank Mark Jarrell, Frank Pinski, and all the other faculty members in the Physics Department for their encouragement and support. I thank Peg Frantz, Lynne McEneny, and all the other staff members in the Physics Department for the courtesy they have shown to me.

I thank the E791 collaboration for giving me an opportunity to participate in an exciting experiment. I enjoyed every moment of E791. I thank Jeff Appel and Milind Purohit for their professional discussions and the support. My special thanks go to Keith Thorne for being my mentor while I was at Fermilab. I enjoyed working with you, and I greatly appreciate what you have done for me. Again, let me thank all the E791 collaborators for the fun time I had at TPL.

Finally, I would like to thank all of you who gave me so much and got so little in return. I may not have mentioned your name, but I have all the good memories written in my heart and will not forget them.

Contents

List of Figures

List of Tables

Chapter 1

Introduction

In this thesis, I am studying the singly Cabibbo suppressed decay $D^0 \to K^0_S K^{\pm}\pi^{\mp}$ and making comparisons with the Cabibbo allowed decay $D^0 \to K^0_S \pi^+\pi^-$. For this analysis I am using about 30% of the data from the E791 experiment, recorded during the 1991 fixed target run at Fermilab. The full E791 data set consists of about 20 billion events originally recorded on about 24,000 Exabyte tapes.

In this chapter I will be looking at the decay $D^0 \to K^0_S K^{\pm}\pi^{\mp}$ from a theoretical point of view. Simple spectator and exchange decay diagrams will be used to look at the sub-structure of the decay $D^0 \to K^0_S K^{\pm}\pi^{\mp}$. I will also give hand-waving arguments to support my expectations based on the simple models.

1.1 The Standard Model

The standard model of electro-weak and strong interactions has been extremely successful in describing the properties of elementary particles. In the standard model the elementary particles of matter, quarks and leptons, are categorized into three families. Each family consists of two quarks, a charged lepton and its neutrino.

$$\text{Quarks}: \begin{pmatrix} u \\ d \end{pmatrix} \qquad \begin{pmatrix} c \\ s \end{pmatrix} \qquad \begin{pmatrix} t \\ b \end{pmatrix}$$

$$\text{Leptons}: \begin{pmatrix} \nu_e \\ e \end{pmatrix} \qquad \begin{pmatrix} \nu_\mu \\ \mu \end{pmatrix} \qquad \begin{pmatrix} \nu_\tau \\ \tau \end{pmatrix}$$

The interactions among the particles are described by three gauge forces, electromagnetic, weak and strong. The electromagnetic and weak interactions are described in a unified manner by the electro-weak theory of Glashow[6], Weinberg[7] and Salam[8]. The four gauge bosons in the electro-weak theory, photon, $W^{\pm}$, and Z^0, mediate the electromagnetic, charged weak and neutral weak forces respectively. Quarks carry an intrinsic quantum number called *color* and each quark can appear in three different colors. Leptons do not carry *color*. The strong force which binds the quarks together arises due to this *color* charge and it is mediated by eight gluons which also carry *color*.

1.1.1 Charged Weak Interactions

The charged weak interactions between the quarks mediated by $W^{\pm}$ couples the quark pairs

$$\begin{pmatrix} u \\ d' \end{pmatrix} \quad \begin{pmatrix} c \\ s' \end{pmatrix} \quad \begin{pmatrix} t \\ b' \end{pmatrix}$$

where d', s' and b' are the weak eigen-states of the physical quarks d, s and b. The couplings between the weak eigen-states and the physical quarks are described by the Cabibbo-Kobayashi-Maskawa(CKM) mixing matrix[9]; a matrix representation of these couplings is shown in equation 1.1.

$$\begin{pmatrix} d' \\ s' \\ b' \end{pmatrix} = \begin{pmatrix} \mathrm{V_{ud}} & \mathrm{V_{us}} & \mathrm{V_{ub}} \\ \mathrm{V_{cd}} & \mathrm{V_{cs}} & \mathrm{V_{cb}} \\ \mathrm{V_{td}} & \mathrm{V_{ts}} & \mathrm{V_{tb}} \end{pmatrix} \begin{pmatrix} d \\ s \\ b \end{pmatrix} \tag{1.1}$$

If one considers only the first two generations, then the CKM matrix can be written using a single angle θ_c, called the Cabibbo angle[10]. In this a case we can write

$\mathrm{V_{ud}} = \cos\theta_c$, $\mathrm{V_{us}} = \sin\theta_c$

$\mathrm{V_{cd}} = -\sin\theta_c$, $\mathrm{V_{cs}} = \cos\theta_c$

where $\sin^2\theta_c \approx 0.05$ [5]

When the $W^{\pm}$ couples to quarks in different generations, the decay amplitudes carry a vertex factor of $\sin\theta_c$ compared to a factor of $\cos\theta_c$ for couplings between the quarks in the same generation. The decay rates are proportional to the squares of the amplitudes and the phase space factors. Therefore, the decay rates of vertices carrying $\sin\theta_c$ terms are suppressed by a factor of $\sin^2\theta_c$ (Cabibbo suppression) compared to the decay rates of vertices carrying $\cos\theta_c$ terms, provided phase space factors are the same.

Furthermore, the $c-d$ quark couplings carry a vertex factor of -$\sin\theta_c$ while the $u-s$ quark couplings carry a vertex factor of +$\sin\theta_c$. Therefore, if a particle can decay into the same final states through two different decay amplitudes that carry +$\sin\theta_c$ and -$\sin\theta_c$ factors, then the decay amplitudes interfere destructively (Glashow, Iliopoulos and Maiani, "GIM" cancellation[11]) to further suppress such decays. To visualize the different signs in this thesis, when drawing Feynman diagrams, the vertices suppressed with a factor $-\sin\theta_c$ are marked with a "$\circ$" and those suppressed with a factor $+\sin\theta_c$ are marked with a "$\bullet$".

1.2 D^0 Decay Mechanisms

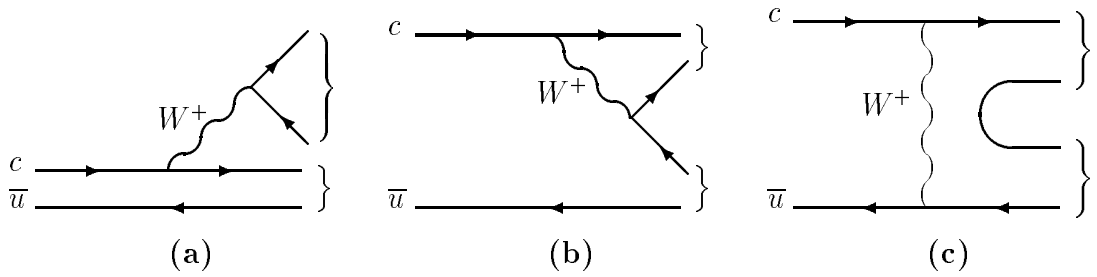

Figure 1.1: Lowest order Feynman diagrams for the D^0 decays: **(a)** spectator decay with external W emission, **(b)** spectator decay with internal W emission, **(c)** W exchange decay. Arrows which point to the right represent quarks and those point to the left represent anti quarks. The curly brackets show the quarks recombining to form final state hadrons.

Figure 1.1 shows tree level non-leptonic Feynman diagrams for D^0 decays. Here I assume that the quarks recombine in the final state to form mesons as shown by the curly brackets. Diagrams (a) and (b) represent spectator decays with external and internal W emission. In spectator decays the charm quark undergoes W emission while the $\overline{u}$ quark remains as a spectator. In external W emission decays, the spectator quark, $\overline{u}$, recombines with the quark coming from the c quark to form final state hadrons. But in the internal W emission decays, the $\overline{u}$ quark recombines with a quark coming from the W decay to form final state hadrons. Diagram (c) represents a W exchange decay. In W exchange decays, quark pairs coming out of the vacuum recombine with the existing quarks to form the final state hadrons.

1.3 The Decay $D^0 \to K^0_S\, K^{\pm}\, \pi^{\mp}$

The decay $D^0 \to K^0_S\, K^{\pm}\, \pi^{\mp}$ is a singly Cabibbo suppressed decay. It can be produced directly with non resonant three body final states or through K^*K quasi-two-body final states as listed below.

- Non-resonant decay $D^0 \to K^0 K^- \pi^+$ with $K^0 \to K^0_S$
- Non-resonant decay $D^0 \to \overline{K}^0 K^+ \pi^-$ with $K^0 \to K^0_S$
- $D^0 \to K^{*+} K^-$ with $K^{*+} \to K^0 \pi^+$ and $K^0 \to K^0_S$
- $D^0 \to K^{*-} K^+$ with $K^{*-} \to \overline{K}^0 \pi^-$ and $K^0 \to K^0_S$
- $D^0 \to \overline{K}^{*0} K^0$ with $\overline{K}^{*0} \to K^- \pi^+$ and $K^0 \to K^0_S$
- $D^0 \to K^{*0} \overline{K}^0$ with $K^{*0} \to K^+ \pi^-$ and $K^0 \to K^0_S$

1.3.1 Spectator Decays

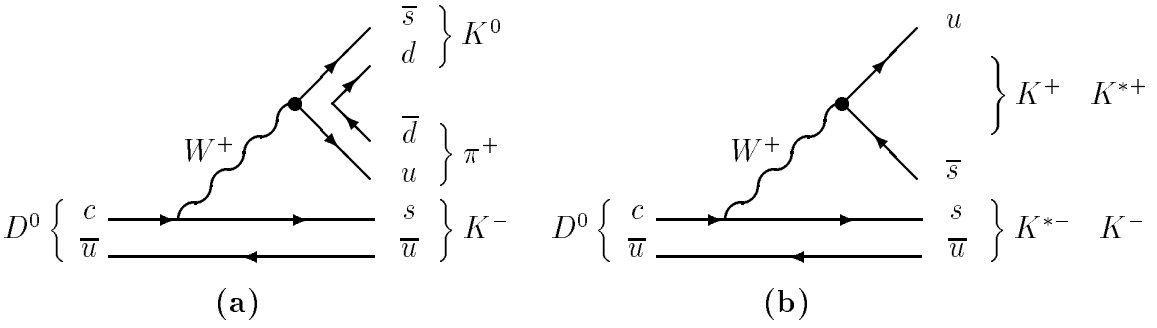

Figure 1.2: Simple spectator decay diagrams that could produce the final state $K^0_S K \pi$. **(a)** Non-resonant production of the $K^0 K^- \pi^+$ final state. One could draw an inner spectator decay diagram producing the decay $K^0 K^+ \pi^-$ as well. **(b)** This resonant decay could produce the quasi two body states $K^+ K^{*-}$ or $K^{*+} K^-$, which could result in the final state $K^0_S K \pi$.

Figure 1.2 shows the lowest order spectator decay Feynman diagrams that could produce the final state $K^0_S K^\pm \pi^\mp$. Non-resonant production of $K^0 K^- \pi^+$ is depicted in Figure 1.2(a). A similar spectator decay diagram could be drawn for the non-resonant production of $\overline{K}^0 K^+ \pi^-$. The decay diagram in Figure 1.2(b) could produce $K^{*+} K^-$ or $K^{*-} K^+$ quasi two body final states. Simple spectator decay diagrams

(ones without final state quark annihilation) will have a $\overline{u}$ quark in the final state. Therefore the simple spectator decay diagrams will not produce the $K^{*0}\overline{K}^0$ or $\overline{K}^{*0}K^0$ two body final states.

The decays $D^0 \to K^{*+}K^-$ and $D^0 \to K^{*-}K^+$ are somewhat similar to the Cabibbo allowed decays $D^0 \to K^-\rho^+$ and $D^0 \to K^{*-}\pi^+$. In the decays $D^0 \to K^{*+}K^-$ and $D^0 \to K^-\rho^+$, the vector boson W decays to vector particles K^{*+} and ρ^+ respectively and in the decays $D^0 \to K^+K^{*-}$ and $D^0 \to K^{*-}\pi^+$, the vector boson W decays to pseudoscalar particles K^+ and π^+ respectively. The branching ratio of $D^0 \to K^-\rho^+$ is larger than that of $D^0 \to K^{*-}\pi^+$ [5]. Therefore, if the same trend extends to the Cabibbo suppressed modes, then we could naively expect the branching ratio of $D^0 \to K^{*+}K^-$ to be larger than that of $D^0 \to K^{*-}K^+$.

Most of the Cabibbo allowed three body decays are predominantly quasi two body decays, even though there is more phase space for non-resonant decays than for resonant two body decays. One could argue that this behavior is due to the fact that final state interactions are playing a much bigger role than phase space in these decays. If the same argument holds for Cabibbo suppressed decays, then we should expect the $D^0 \to K^0_S K\pi$ non-resonant decay rates to be smaller than those of $D^0 \to K^{*+}K^-$ and $D^0 \to K^+K^{*-}$.

1.3.2 Exchange Decays

Figure 1.3 show the simplest $W^\pm$ exchange Feynman diagrams contributing to the decay $D^0 \to K_s\, K^\pm\, \pi^\mp$. The exchange decay of Figure 1.3 could produce any of the quasi-two-body final states, $K^{*+}K^-, K^+K^{*-}, K^{*0}\overline{K^0}$ or $K^0\overline{K^{*0}}$, while the exchange decay of Figure 1.3 is only capable of producing the $K^{*0}\overline{K^0}$ or $K^0\overline{K^{*0}}$ final states.

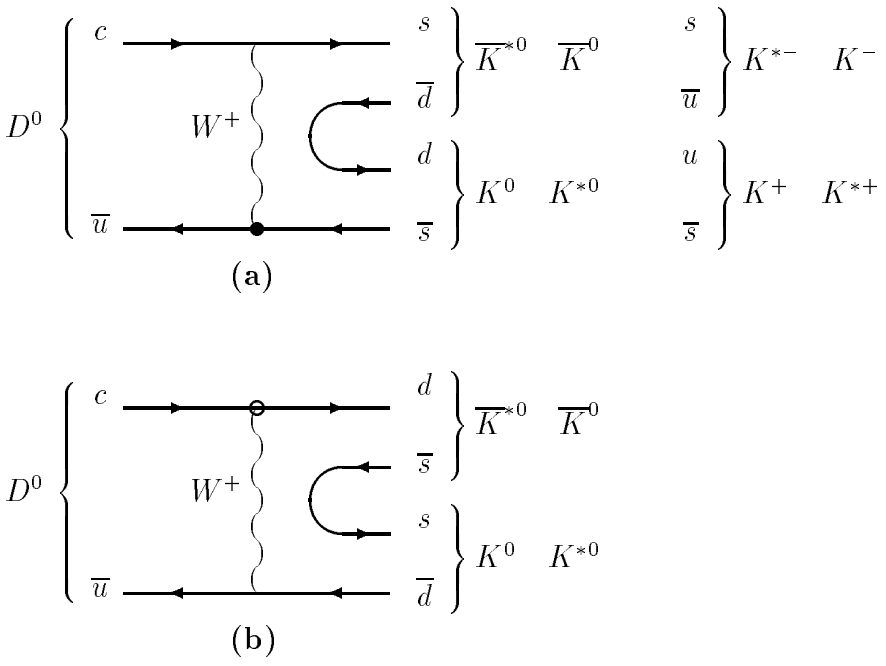

Figure 1.3: Simplest exchange decay diagrams that could produce the final states $K^0_S K^{\pm}\pi^{\mp}$. **(a)** This decay diagram is suppressed by a vertex factor $+\sin\theta_c$ and could produce any of the quasi two body final states $K^{*+}K^-$, K^+K^{*-}, $\overline{K}^{*0}K^0$ or $K^{*0}\overline{K}^0$. **(b)** This decay diagram is suppressed by a vertex factor -$\sin\theta_c$ and could produce only the quasi two body final states $\overline{K}^{*0}K^0$ or $K^{*0}\overline{K}^0$. The decay amplitudes from this diagram interfere destructively with those from **1.3a**.

Identical final states of the Feynman diagrams in Figures 1.3(a) and 1.3(b) carry identical phase space factors; the corresponding decay amplitudes are equal in magnitude except for a difference in the overall sign due to the vertex factors of $+\sin\theta_c$ and $-\sin\theta_c$. Therefore, due to GIM cancellation, the decay rates of $D^0 \to K^{*0}\overline{K^0}$ and $D^0 \to K^0\overline{K^{*0}}$ will be suppressed further than other Cabibbo suppressed decay rates. One can also draw two decay diagrams similar to the two in Figure 1.3 with two pairs of quarks emerging out of the vacuum instead of one, producing the non-resonant $K^0_S K^{\pm}\pi^{\mp}$ final states. Such decay amplitudes will also be suppressed by the GIM cancellation.

1.3.3 Putting Things in Prospective

Table 1.1 shows a summary of the contributions of different Feynman diagrams to resonant and non-resonant sub-structure of the decay $D^0 \to K^0_S K^{\pm}\pi^{\mp}$.

Non-Resonant decays	$K^{*+}K^-/K^+K^{*-}$ decays	$\overline{K}^{*0}K^0/K^{*0}\overline{K}^0$ decays
produced by spectator	produced by spectator	not produced by spectator
produced by W exchange	produced by W exchange	produced by W exchange
exchange decay GIM suppressed	exchange decay NOT GIM suppressed	exchange decay GIM suppressed

Table 1.1: Summary of the contribution of spectator and exchange decay diagrams to resonant and non-resonant sub-structure of the decay $D^0 \to K^0_S K^{\pm}\pi^{\mp}$

One can summarize the expectations based on the arguments given earlier in this chapter as follows:

- $K^{*+}K^-/K^+K^{*-}$ should be produced at a larger rate compared to the other two modes,
- $K^{*+}K^-$ resonance to be favored over K^+K^{*-},
- The non-resonant decay rates to be smaller than those of $K^{*+}K^-$ and K^+K^{*-}, and
- $\overline{K}^{*0}K^0/K^{*0}\overline{K}^0$ rates be the smallest.

Chapter 2

The E791 Experiment

The E791 experiment was designed to collect a large sample of events enriched with "charmed" particles. This was a second generation hadro-production experiment done in the Tagged Photon Laboratory (TPL) at Fermilab. It took data during the 1991 fixed target run at Fermilab with a 500 Gev π^- beam and collected an unprecedented data sample of 20 billion events using a very loose trigger based on the charge multiplicity and transverse energy E_T. I have used 170 runs worth of data out of a total of 575 runs to obtain the results presented in this thesis.

In this chapter I have included discussions of the TPL spectrometer used for the E791 experiment, data-taking, and the reconstruction of tracks and vertices. The track and vertex reconstruction descriptions in this thesis refer to the release 5 version of the E791 offline software package, unless otherwise noted.

2.1 TPL Spectrometer

The main components of the TPL spectrometer downstream of the target include Silicon Microstrip Detectors (SMD) for precision tracking and vertex reconstruction,

drift chambers (DC) and proportional wire chambers (PWC) for downstream tracking, two magnets (M1 & M2) for track momentum measurements, two threshold Čerenkov counters (C1 & C2) for particle identification, electromagnetic and hadronic calorimeters for particle energy measurements, and two muon walls for muon identification. A beam tracking system consisting of SMD and PWC planes located upstream of the target was used for precision measurements of the transverse position of the beam particles. A schematic of the yz cross-section of the TPL spectrometer used for the E791 experiment is shown in Figure 2.1. This figure is drawn out of proportion to visualize all the parts of the detector. Several major changes were made to the experimental setup at the TPL since it was used by E769, the predecessor of the E791 experiment. The addition of more SMD planes to both upstream and downstream tracking systems and the introduction of a very fast data acquisition (DA) system were the most important changes for the analysis described in this in this thesis.

2.1.1 The E791 Coordinate System

As with any experiment, E791 had its own coordinate system. The z axis in the E791 coordinate system extended from South to North, very close to the direction of the beam. The x axis extended from East to West and the y axis pointed from the ground up. The three axis formed a mutually perpendicular right handed coordinate system. Additionally, the u, v, w and w' directions were defined as follows: The u direction was defined to be at an angle of $+20.5$ degrees from the positive x direction towards the positive y direction; the v direction was defined to be at an angle of 20.5 degrees from the positive x direction towards the negative y direction;

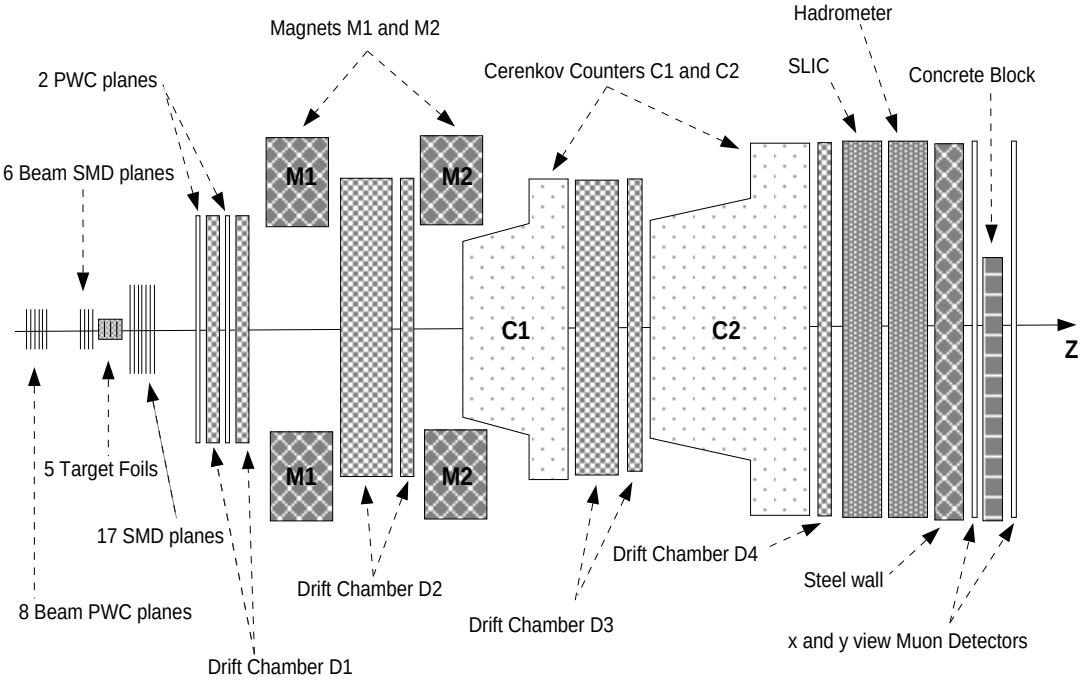

Figure 2.1: A schematic of the yz cross-section of the TPL spectrometer used for the E791 experiment. This is not drawn to scale.

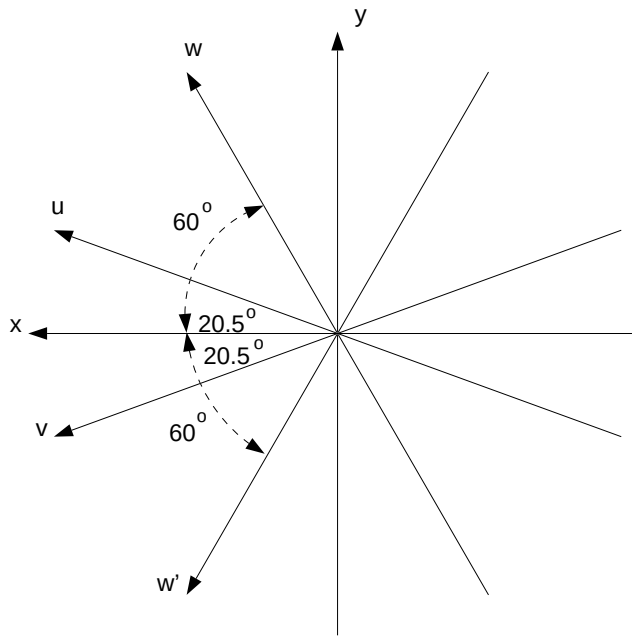

Figure 2.2: Axis in the E791 coordinate system. z axis is going into the paper at the center of other axis; x and y axis are perpendicular to each other; the angles (in degrees) between the positive x direction and the positive direction of other axis are shown in the diagram.

the w direction was defined to be at an angle of 60 degrees from the positive x direction towards the positive y direction; and the w' direction was defined to be at an angle of 60 degrees from the positive x direction towards the negative y direction. All the detectors of the spectrometer were approximately centered around the z axis. As a convention, centimeters were used to measure lengths.

2.1.2 Beam Tracking System

In E791 the transverse positions of beam particles prior to interacting with the target were measured using eight PWC and six SMD planes. PWC planes were located about 30 meters upstream of the target to provide good angular resolution, and the SMD planes were located close to the target to provide good spatial resolution. PWC

	First PWC station	Second PWC station
Number of planes	4	4
Dimensions(cm)	6x3	6x3
View ordering	X, X', Y, W	X, X', Y, W
Wire spacing(mm)	1.0	1.0
Resolution(μm)	145(X, X');289(Y, W')	145(X, X');289(Y, W')
Location in z (cm)	-3117.0 to -3116.0	-1211.0 to -1209.0

Table 2.1: Characteristics of the PWC planes in the beam tracking system

	First SMD station	Second SMD station
Number of planes	3	3
Dimensions(cm)	5x5	5x5
View ordering	Y, X, W'	W', X, Y
Efficiency(%)	85, 85, 98	98, 98, 98
Strip pitch(μm)	25	25
Resolution(μm)	7.2	7.2
Location in z (cm)	-80.25 to -74.52	-33.163 to -29.483

Table 2.2: Characteristics of the SMD planes in the beam tracking system

planes were grouped into two stations and their characteristics are listed in Table 2.1. Table 2.2 shows the characteristics of the SMD planes, which were also grouped into two stations.

2.1.3 Target

The target used for the E791 experiment consisted of 5 circular foils held in place with plexiglas spacers; details of the target are given in Table 2.3. The most upstream target foil was made of platinum and the other four foils were made of carbon (synthetic diamond). Target foils were spaced by about 1.5 cm to maximize the fraction of short lived particles decaying in free space.

Target Number	1	2	3	4	5
Material	Platinum	Carbon	Carbon	Carbon	Carbon
Thickness(cm)	0.052	0.1572	0.1567	0.1530	0.1544
Diameter(cm)	1.606	1.369	1.377	1.368	1.355
Mass (grams)	2.2396	0.7490	0.7507	0.7373	0.7300
Density (gr/cc)	21.3	3.24	3.22	3.28	3.28
Radiation Lengths	0.169	0.012	0.012	0.012	0.012
Proton Interaction Lengths[1]	0.00584	0.00590	0.00585	0.00582	0.00587
Z coordinate(cm)	-8.191	-6.690	-5.154	-3.594	-2.060

Table 2.3: E791 target information. The number of pion interaction lengths is about 2/3 of the proton interaction lengths.

2.1.4 Downstream SMD Planes

The D^0 lifetime is $(4.21 \pm 0.10) \times 10^{-13}$ seconds [5]. A D^0-meson produced with a momentum of 100 GeV would travel about 0.7 cm in the lab before decaying. Therefore, to separate the primary vertices from the secondary vertices, detectors with high spatial resolutions are a must. To achieve this goal, we used 17 SMD planes in the downstream tracking system. The overall geometrical acceptance of the SMD system was about $\pm$150 milliradians around the beam axis. The pitch of the SMD planes varied from 25 μm for inner strips of the upstream planes to 200 μm for the outer strips of the downstream planes. The transverse resolution of the SMD system was typically in the order of 15 μm when the tracks were projected back to the origin. The efficiencies of the SMD planes ranged from 83% for the upstream planes to 99% for the downstream planes. The detailed characteristics of the downstream SMD planes are listed in the Table 2.4.

Plane	z position(cm)	strip pitch(μm)	Efficiency(%)	View
1	0.670	25 ; 50	83	Y
2	1.000	25 ; 50	85	X
3	1.931	25 ; 50	93	X
4	3.015	50 ; 50	95	Y
5	6.684	50 ; 50	96	V
6	11.046	50 ; 50	98	Y
7	11.342	50 ; 50	97	X
8	14.956	50 ; 50	94	V
9	19.915	50 ; 50	90	X
10	20.254	50 ; 50	88	Y
11	23.878	50 ; 50	93	V
12	27.558	50 ; 200	98	V
13	31.848	50 ; 200	96	X
14	34.548	50 ; 200	98	Y
15	37.248	50 ; 200	99	X
16	39.948	50 ; 200	99	Y
17	45.508	50 ; 200	99	V

Table 2.4: Characteristics of the downstream SMD planes. The inner strips of some of the SMD planes had a different pitch than that of the outer strips. The two numbers given for pitch are that for the inner strips and for the outer strips respectively.

2.1.5 Drift Chambers

There were 35 drift chamber planes in the TPL spectrometer. They were the main components of the downstream charged track detection system. Drift chamber planes were divided into four modules: D1, D2, D3 and D4. Each of the drift chamber modules consisted of several assemblies with three or four drift chamber planes in each of them. Drift chamber resolutions varied from about 260 μm for D3 to 500 μm for D4. The average efficiency of the drift chambers was about 92%. Detailed information about the drift chambers are listed in Table 2.5.

	D1	D2	D3	D4
Approximate dimensions (cm)	130 x 75	280 x 140	320 x 140	500 x 250
u and v cell size (cm)	0.446	0.892	1.487	2.974
x cell size (cm)	0.476	0.953	1.588	3.175
Number of assemblies	2	4	4	1
Total number of planes	8	12	12	3
View ordering	x, x', u, v	u, x, v	u, x, v	u, x, v
z position of first plane (cm)	142.5	381.4	928.1	1738.0
z position of last plane (cm)	183.7	500.8	1047.1	1749.2
Approximate resolution (μm)	430	320	260	500
Approximate efficiency	92%	93%	93%	90%

Table 2.5: Characteristics of the drift chamber system

2.1.6 Downstream PWC Planes

The two downstream PWC planes were added to the TPL spectrometer to be used in track reconstruction. They were located at 120.4 cm and 162.94 cm in z. Both of these planes measured the y coordinate of the tracks and had a wire spacing of 2.0 mm. The resolution of these two planes was measured to be about 750 μm.

2.1.7 Magnets

The TPL spectrometer had two magnets, M1 and M2. The major component of the magnetic field (B_y) was aligned anti-parallel to the y direction in the E791 coordinate system. The maximum magnitude of B_y was about 5 kG in the magnet M1 and 7 kG in the magnet M2; average total integrated magnetic field strength ($\int \vec{B}_y \times \vec{dz}$) was about 17.5 kG meters. The approximate P_T kicks of the magnets M1 and M2 were 0.212 GeV/c and 0.324 GeV/c respectively.

Figure 2.3 shows an xy cross-section of the TPL magnets including the mirror plates. The z coordinates of the magnets and mirror plates are shown at the bottom of the figure. This diagram is drawn to scale. Please refer to Table 2.6 for a complete list of dimensions of the magnets.

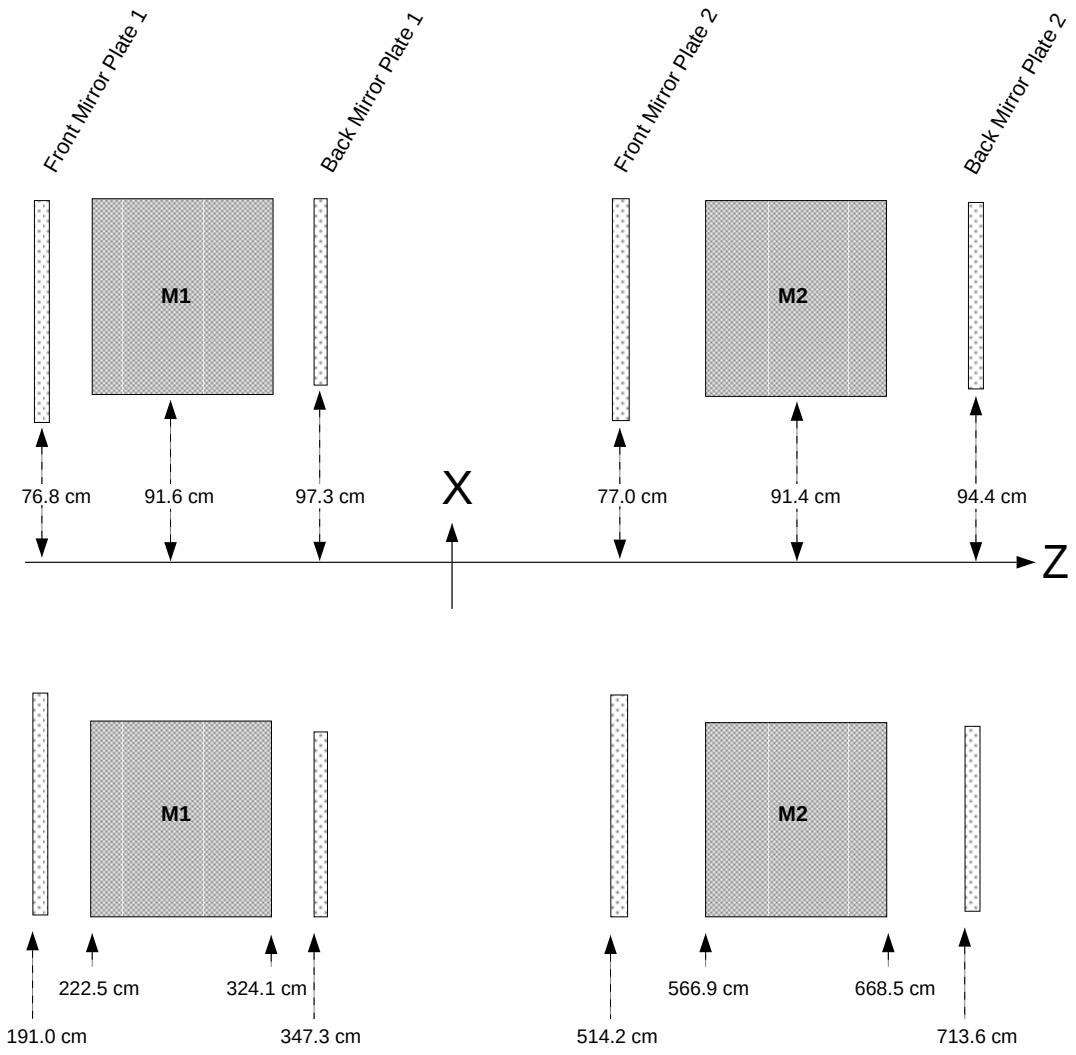

Figure 2.3: An xz view of the TPL magnets drawn to scale. The magnitudes of the apertures shown here are half the full widths. The z coordinates of the magnets and mirror plates are shown at the bottom of the figure.

Device	x Aperture in cm	y Aperture in cm	Upstream z in cm	Downstream z in cm
Front Mirror Plate 1	76.8	36.3	191.0	199.0
Magnet M1	91.6	40.5	222.5	324.1
Back Mirror Plate 1	97.3	48.6	347.3	355.1
Front Mirror Plate 2	77.0	36.9	514.2	522.1
Magnet M2	91.4	42.8	566.9	668.5
Back Mirror Plate 2	94.4	51.3	713.6	721.5

Table 2.6: Dimensions of the TPL Magnets. The magnitudes of the apertures listed, are half the full widths.

2.1.8 Čerenkov Counters

The two threshold Čerenkov counters (C1 and C2) in the TPL spectrometer were used for identifying pions, kaons, and protons. A detailed description including the threshold curves of these Čerenkov detectors can be found in reference [12]. C1 was filled with nitrogen and C2 was filled a mixture of 20% nitrogen and 80% helium. Gases in both Čerenkov counters were maintained at atmospheric pressure. Because of the different gas mixtures used in the counters C1 and C2, the minimum momentum of a particle required to trigger the two counters are different. The threshold momenta for pions, kaons, and protons are listed in Table 2.7. These numbers were initially calculated, and then confirmed using data.

	C1	C2
Pion momentum threshold (GeV/c)	6	11
kaon momentum threshold (GeV/c)	20	36
Proton momentum threshold (GeV/c)	38	69

Table 2.7: The minimum threshold momenta for pions, kaons and protons to trigger the Čerenkov counters C1 and C2

2.1.9 Calorimeters

The TPL spectrometer had two sampling calorimeters, a Segmented Liquid Ionization Calorimeter (SLIC) for measuring the energy of electrons and photons, and a Hadronic Calorimeter (Hadrometer) for measuring the energy of charged and neutral hadrons[13, 14]. These calorimeters were used as a part of the E791 trigger to select the events with a mild transverse energy (E_T) requirement[2]. The information from the calorimeters was also used as part of the particle identification system to separate electrons, photons, muons and hadrons. A more complete discussion of the TPL calorimeters used for E791 can be found in reference [13].

2.2 Trigger Selection and Data Acquisition

With the on-line computing resources available when the data were taken, real time identification of events with charmed particles was extremely difficult. Therefore, E791 decided to collect as much data as it could with very loose constraints, and then to analyze the events when time and computing resources were available.

The E791 trigger consisted of two parts, a pre-trigger which was based on the quality of the beam and a secondary trigger based on the decay products. The pre-trigger selection required that there be only one beam particle and no stray beam particles present. The secondary trigger required that there be at least four charged tracks produced in the interaction of the beam particle in the target region and the minimum total transverse energy (E_T) of the event be few (≈ 4.5) GeV. About 85% of the events passing the minimum charged track requirement in the secondary trigger satisfied the E_T requirement as well.

Because of the loose trigger selection, events had to be recorded at a very high

[2] A minimum E_T of about 4.5 GeV

rate. Therefore, the data acquisition (DA) system at TPL was rebuilt for the E791 experiment. The modified DA system read out 24000 channels in 50 μsec. Events were accepted at the rate of 9000 per second. Eight large first-in first-out (FIFO) buffers were used to store event segments, which were then compressed and formatted by 54 ACP 1 processors housed in 6 VME crates. Data was written continuously to 42 Exabyte tape drives at the rate of 9.6 Mb/sec. It took about 2.5 hours to fill a set of 42 Exabyte tapes (one run). Please see reference [15] for a more complete description of the E791 DA system.

2.3 Track Reconstruction

In E791, we first reconstruct the beam track, which is upstream of the target, and then the tracks downstream of the target. Beam tracks are reconstructed using the hits from the upstream PWC and SMD planes[3]. All possible straight lines are formed using these hits; only the best track, based on the χ^2 and the number of hits, is kept. The beam track reconstruction efficiency is about 95%.

Then the tracks found within the 17 downstream SMD planes are reconstructed. We start the SMD track reconstruction by finding all the single view tracks in each of the views x, y and v. Then the three view tracks are formed from the single view tracks. Next the three view tracks are ordered in the descending order of their quality, which is a function of the total number of hits, the number of unique hits, and the χ^2 of the tracks. Starting with the best three view SMD track, an attempt is made to continue these tracks into the drift chamber system.

Drift chamber track reconstruction algorithm uses what we call *triplets*, to locate the (x, y) positions of the track candidates within drift chambers. The drift chambers

[3]see section 2.1.2 for details about these detectors

D2, D3, and D4 are arranged in groups of u, x and v view planes placed very closely in z, close enough to assume the same value of z for all three planes. Let us imagine a picture, where all the u, x and v wires from a given group are projected on to a xy plane at this z. The point of intersection of three wires each from u, x and v view planes defines a triplet; wires may not necessarily have a single point of intersection; it is sufficient for the wires to go close to each other within the resolution of the drift chamber to form a triplet. Due to the left right ambiguity of drift chamber hits, we can have up to eight hit triplets for each wire triplet. All the triplets in drift chambers D2, D3 and D4 are formed at the beginning of the track reconstruction program.

To link the SMD track segments with the drift chamber track segments we project the SMD track segments in straight lines in the y view[4] to search for matching triplets in D3. To allow for multiple scattering, a window of about ± 2.5 cm in y is used. If any matching triplets are found, using each triplet's position, the slopes and the intercepts of the SMD track segment, and a *single bend point approximation* for the magnetic field, a road is defined. In the *single bend point approximation*, the transverse momentum kick, P_T, of the magnet is assumed to be concentrated at the center of the magnet; charged tracks going through the magnet bend only once, at the center of the magnet. The roads defined here are typically few millimeters wide; the exact size depends on the momentum of the track. Once a road is defined, the tracking code searches the road for additional triplets and hits in D3. If at least eight hits are found in D3, then the search for additional hits in the road is continued to D2. Again, if at least eight hits are found in D2 then the road is extended to D1 and D4 in search of additional hits. Finally, the track candidates are fitted using a χ^2 minimization routine to determine the slopes, intercepts, and momenta. Tracks with a χ^2/ν less than 5 are kept. The SMD segments, drift chamber triplets and hits used

[4]The major component of the magnetic field is in the y direction; therefore, tracks are expected to be straight lines in the y view.

by the good tracks are marked as unavailable to be used in later tracks. This process is repeated using the remaining SMD track segments and the remaining triplets in D2. The tracks found here, with SMD and drift chamber hits, are called SESTR tracks.

Due to SMD inefficiencies, not all real tracks which pass through the SMD system are reconstructed as SESTR tracks. Also, a majority of the K^0_Ss and Λs decay downstream of the SMD system. At this stage, these tracks are reconstructed using only the drift chamber hits (ESTR tracks). The ESTR tracking begins by forming pairs of triplets in D3. For each pair of triplets, a road within D3 is defined. These roads are typically few millimeters wide; the exact size depends on the momentum of the track. Once the road is defined, the ESTR tracking code searches the road for additional triplets and hits in between and beyond the two triplets. If at least eight hits are found in D3, then the road is projected to D2 in the y view and searched for matching triplets. If any triplets are found, using that triplet's (x, y) position, the slopes and the intercepts of the D3 track segment, and using a single bend point approximation, a road within D2 is defined. If at least eight hits are found within the D2 road, then the road is extended to D1 and D4 in search of more hits. Finally, the tracks are fitted using a χ^2 minimization routine to determine the slopes, intercepts and the momenta. The tracks with a χ^2 per degree of freedom less than 5 are kept. Just as before, the drift chamber triplets and hits used by the good tracks are marked as unavailable for later tracks. To complete this exhaustive search for ESTR tracks, a similar track reconstruction attempt is made by starting with the remaining triplets in D2.

2.3.1 Track Categories

For the convenience of identifying tracks with different drift chamber hits, we assign a track category number to each one. In this scheme, the bits 0, 1, 2 and 3 are assigned to tracks with hits in D1, D2, D3 and D4 respectively. For example, if a track has only D1 and D2 drift chamber hits, then its category is defined as 3 (2^0+2^1). Similarly, the category of a track with segments in D1, D2, D3 and D4 is defined as 15 ($2^0 + 2^1 + 2^2 + 2^3$). A detailed listing of the commonly used track categories is in Table 2.8. Additionally, the tracks with only SMD hits are assigned the category 0, and tracks with only SMD and D1 hits are assigned the category 1.

Hits in the track	Category
Only SMD hits	0
Only SMD and D1 hits	1
D1 and D2 hits, possible to have SMD hits as well	3
Only D2 and D3 hits	6
D1, D2 and D3 hits, possible to have SMD hits as well	7
Only D2, D3 and D4 hits	14
D1, D2, D3 and D4 hits, possible to have SMD hits as well	15

Table 2.8: Definition of the track categories. Category 3, 7, and 15 tracks can also have SMD hits.

2.3.2 Track Reconstruction Efficiency

I measured the track reconstruction efficiency[5] using $D^0 \to K^0_S\pi\pi$ Monte Carlo events. The tracks coming from K^0_Ss decaying between 10 cm and 142 cm were used to measure the ESTR track reconstruction efficiency. SESTR track reconstruction efficiency was measured using the two pion tracks in $D^0 \to K^0_S\pi\pi$, that do not come from the K^0_S. Monte Carlo tracks coming from D^0s were matched to the reconstructed tracks

[5]The track reconstruction efficiency is the fraction of the tracks within the acceptance of the spectrometer that were correctly reconstructed

using the slopes, intercepts at $z = 0$ and momenta. The track with the smallest difference in slope and passing the intercept and momenta difference requirements was taken as the matched track. The slope and intercept requirements used for matching SESTR tracks were different from those used to match ESTR tracks, because of the the difference in resolutions of SMDs and drift chambers. The momenta of the matched tracks were required to be within 4% of the true momenta and the slope and intercept requirements used for track matching are listed in Table 2.9.

	SESTR tracks	ESTR tracks
Slope in x (mrad)	1	4
Slope in y (mrad)	1	4
Intercept in x (cm)	0.01	0.40
Intercept in y (cm)	0.01	0.40

Table 2.9: Maximum allowed differences of slopes and intercepts used for track matching.

From this study I found the SESTR track reconstruction efficiency to be around 87% and the ESTR track reconstruction efficiency to be around 59%. Since the ESTR tracks require two triplets compared to a single triplet required for SESTR tracks, the ESTR track reconstruction efficiency is expected to be lower than that for SESTR tracks.

It seems that the ESTR track reconstruction efficiency found in this Monte Carlo is unrealistically low. This might be a problem in the Monte Carlo, and has to be investigated. However, I am not using the absolute values of track or K^0_S reconstruction efficiencies; when I compare the decays $D^0 \to K^0_S K\pi$ and $D^0 \to K^0_S \pi\pi$, I expect the these inefficiencies to cancel.

2.4 Vertex Reconstruction and the *Vertex List*

Vertices are formed from tracks with a common intersection point. In E791, a list of vertices formed with SESTR tracks (*vertex list*) is created at reconstruction time. This vertex reconstruction algorithm starts by forming the primary vertex which is very heavily weighted to include the beam track and constrained to be inside one of the target foils. Then, using the SESTR tracks that are not in the primary vertex, attempts are made to form separated vertices starting from higher multiplicity ones and working the way down. Track sharing among the vertices is very heavily discouraged.

This algorithm was not designed to find all possible vertices. Its design purpose was to reconstruct the primary vertex and to assure us that all events with a secondary vertex would be found as having at least one secondary vertex. The primary vertex reconstruction efficiency of this algorithm is about 95%. The secondary vertex reconstruction efficiency decreases with the decreasing vertex separation. From the Monte Carlo studies I did with the decay $D^0 \to K^0_S K\pi$, I found that the reconstruction efficiency of the $K\pi$ vertices[6] is about 16% for a SDZ cut[7] of 13 which is a typical SDZ cut used in the analysis described in this thesis. (The exact value of the SDZ cut is more complicated as explained in section 4.1.) This low efficiency is mainly due to the fact that most of the $K\pi$ vertices were produced at low vertex separations. The vertex reconstruction efficiency depends on the decay mode ($K^{*+}K^-$, $\overline{K}^{*0}K^0$, non-resonant $K^0_S K\pi$, or $K^0_S\pi\pi$) as well. Please see appendix E for more details on vertex reconstruction efficiency.

[6] The efficiency for the $K\pi$ vertices from the decay $D^0 \to K^0_S K\pi$ to appear as two prong vertices in the vertex list, once the two tracks are correctly reconstructed

[7] See section 3.1.2 for a description of the SDZ cut

Chapter 3

An Introduction to the Analysis

In this thesis I am studying the sub-structure of the decay $D^0 \to K^0_S K\pi$ and making comparisons with the decay $D^0 \to K^0_S \pi\pi$. Due to the enormous size of the E791 data set, several selection stages are required to obtain a reasonably sized sample to do a physics analysis. In E791, the first selection stage is called *filtering*, and the next selection stages are called *stripping*, *sub-stripping*, etc. At the filtering stage we use very mild cuts to select events with secondary vertices and write those events to the data summary tapes (DSTs). Currently, our filtering code passes about 18% of the input events. In the next stage, $D^0 \to K^0_S K\pi$ and $D^0 \to K^0_S \pi\pi$ candidates are stripped as explained in section 3.5.

3.1 Techniques Used to Find D^0 Candidates

I used the following techniques to isolate D^0 candidates:

1. Point back cut,
2. Vertex separation, and
3. D^* hypothesis.

3.1.1 The Point Back (DIP) Cut

In an ideal situation, the trajectories of each daughter particle in a decay should point back to the vertex of the parent particle. Similarly, the trajectory of a composite parent should point back to the decay vertex of the grandparent. In reality, the reconstructed trajectories do not point back perfectly due to measurement errors. In E791 terminology, how well a trajectory of a particle points back to a vertex is measured quantitatively using the variable DIP. It is defined as the distance of closest approach between the vertex and the particle's trajectory.

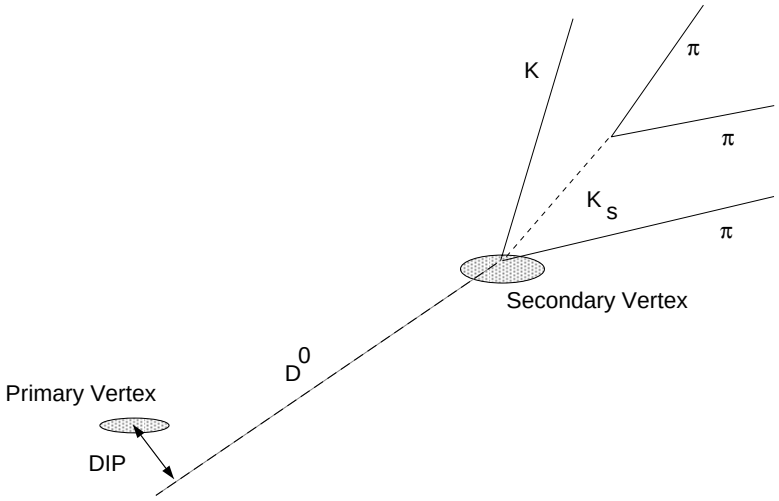

Figure 3.1: DIP of a D^0 candidate with respect to the primary vertex for a decay $D^0 \rightarrow K^0_S K\pi$. The reconstructed D^0 trajectory is projected back from its decay vertex towards its production vertex. DIP of the D^0 with respect to the primary vertex is the perpendicular distance from the primary vertex to the projected D^0 trajectory.

Figure 3.1 shows the DIP of a D^0 candidate with respect to the primary vertex for a $D^0 \rightarrow K^0_S K\pi$ decay, with the K^0_S decaying to two pions.[1] Before the DIP can be

[1]This is a more complex case of the simpler situation where a single daughter track point back to its parents decay vertex.

calculated, the parent particle's trajectory has to be reconstructed. This is done by finding the total momentum of the parent particle and then projecting in a straight line upstream from the parent particle's decay vertex towards its production vertex. DIP with respect to the production vertex is the distance of closest approach between the parent particle's trajectory and the production vertex.

Figure 3.2 shows the distributions of DIP with respect to the primary vertex for the $D^0 \to K^0_S\pi\pi$ candidates. Figure 3.2(a) is from Monte Carlo signal events. Figure 3.2(b) is from real data which is primarily background. In this analysis, the DIP of D^0 candidates with respect to the primary vertex was required to be less than about 50 μm typically. (The exact value of the DIP cut depended on few other factors as explained in section 4.1.) Compared to a cut at 80 μm which is almost 100% efficient, this cut reduced the background by about a factor of two while keeping 92% of the signal.

3.1.2 The Vertex Separation (SDZ) Cut

In E791, separation of primary and secondary vertices was measured quantitatively using the variable SDZ. It was defined as

$$\mathrm{SDZ} = \frac{\Delta \mathrm{Z}}{\sigma_{\mathrm{z}}}$$

where ΔZ is the separation between the primary and the secondary vertices in the z direction and σ_z is the error of ΔZ. The SDZ for a typical decay is graphically depicted in Figure 3.3.

Figure 3.4 shows the distributions of SDZ for the $D^0 \to K^0_S\pi\pi$ candidates. Figure 3.4(a) is from Monte Carlo events. Figure 3.4(b) is from real data which is primarily background. In this thesis the SDZ of D^0 candidates was typically required to be

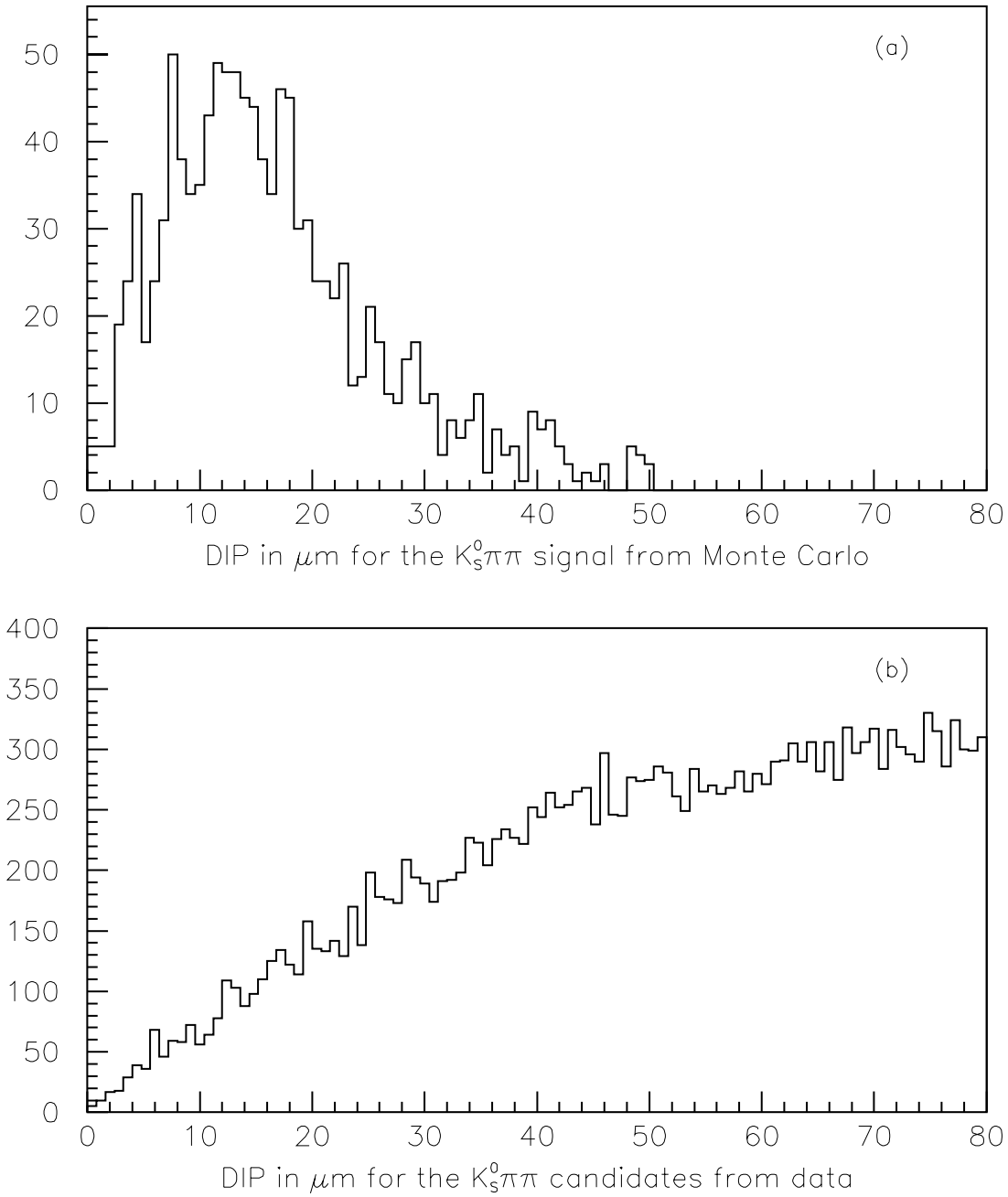

Figure 3.2: The distribution of DIP of $D^0 \to K^0_s\,\pi\,\pi$ candidates with respect to the primary vertex. **(a)** DIP from Monte Carlo signal events. **(b)** DIP from data which is primarily background.

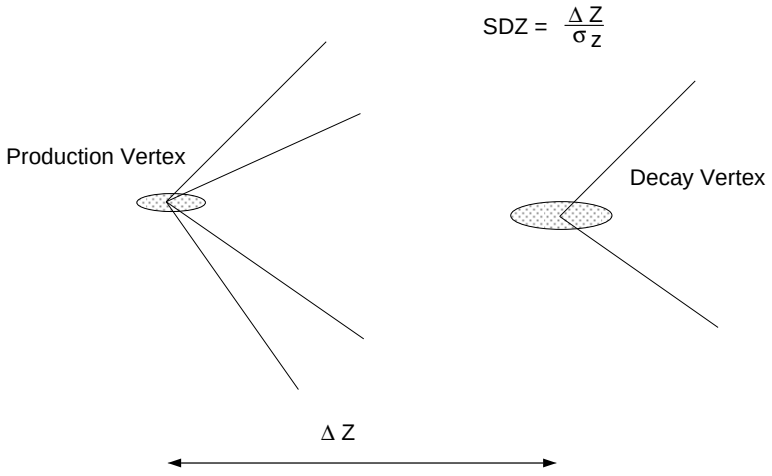

Figure 3.3: SDZ for a typical decay

greater than 13. (The exact value of the SDZ cut depended on few other factors as explained in section 4.1.)

3.1.3 The D^* Hypothesis

In parts of the analysis, I required that the D^0 candidates come from a D^* through the decay $D^{*+} \rightarrow D^0\pi^+$. To satisfy this hypothesis, the D^*-D^0 mass difference was required to be within 1.5 MeV of the nominal $D^* - D^0$ mass difference of 145.44 MeV [5]. Selecting events with this hypothesis served the two purposes: to separate D^0 candidates from $\overline{D}^0$ candidates and to suppress background.

The final state $K^0_S K\pi$ can be realized through the decay $D^0 \rightarrow K^0_S K^+\pi^-$, through the decay $D^0 \rightarrow K^0_S K^-\pi^+$, or through the charge conjugate decays of the above two. We could separate D^0 candidates from $\overline{D}^0$ candidates by looking at the charge of the pion from the $D^{*\pm}$ decay[2] when the D^0 or the $\overline{D}^0$ candidate is coming from a $D^{*\pm}$.

Also, requiring the D^0 to obey the D^* hypothesis reduced the combinatorial back-

[2] $D^{*+} \rightarrow D^0\pi^+$ and $D^{*-} \rightarrow \overline{D}^0\pi^-$

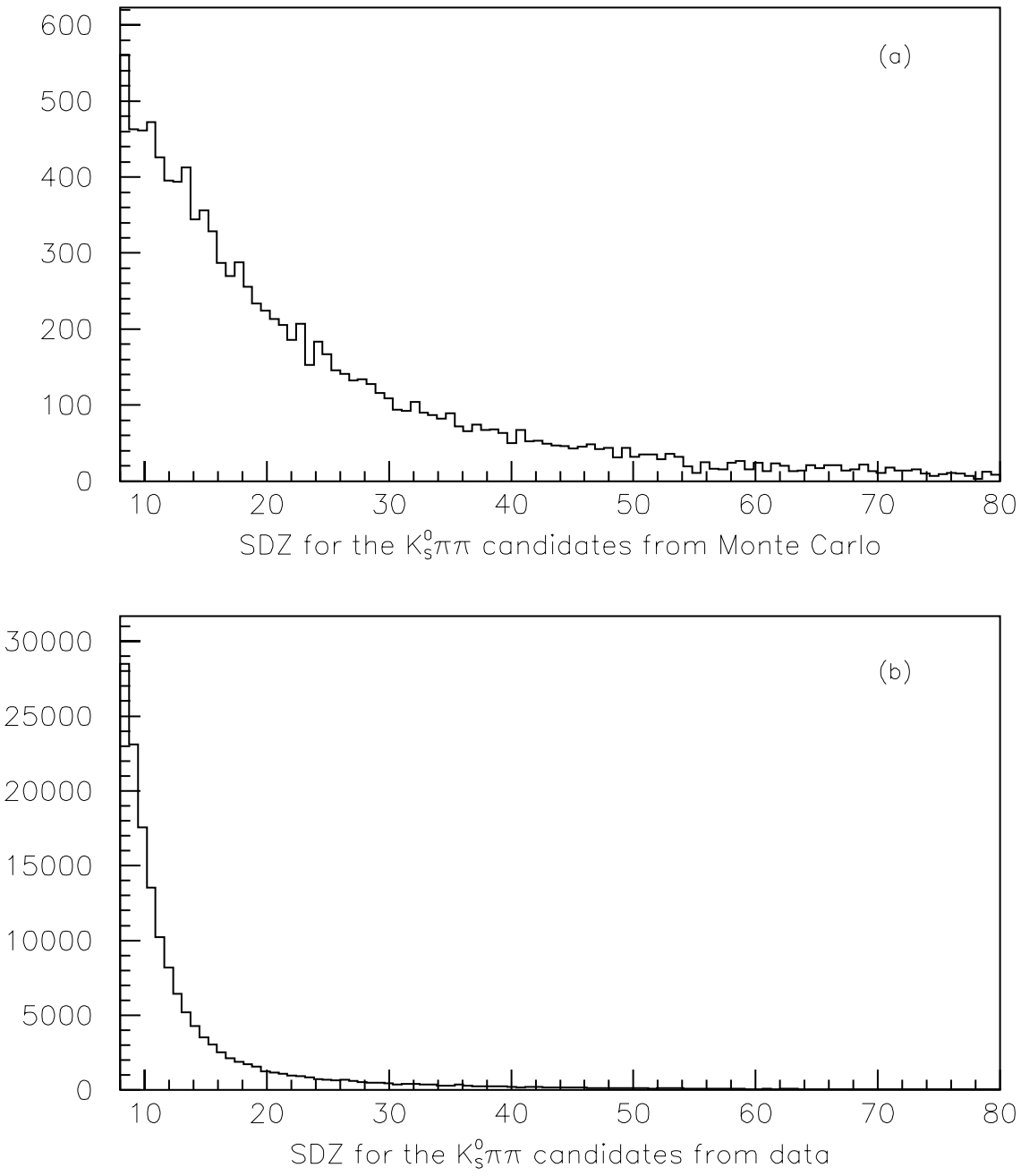

Figure 3.4: SDZ of the D^0 candidates assuming the decay $D^0 \to K^0_s\pi\pi$. **(a)** SDZ from Monte Carlo events. **(b)** SDZ from data which is primarily background.

ground by a factor of about 50 while losing about 25% of the true D^* events.

3.2 Reconstruction of K^0_S Candidates

The decays I am looking for have K^0_S candidates in the final state. Therefore, the K^0_S reconstruction is important to this analysis. About 68% of the K^0_Ss decay to two charged pions and about 31% decay to two neutral pions. We do not reconstruct neutral pions in E791. Therefore, only the K^0_S candidates that decay to two charged pions are reconstructed and used in this analysis. On average, about 4.2% of the original events contained reconstructed K^0_Ss. About 14% of these K^0_S candidates were reconstructed from using two SESTR tracks and 86% were reconstructed using two ESTR tracks. Due to very high combinatorial backgrounds, K^0_S candidates reconstructed from the combinations of SESTR and ESTR tracks were not used in this analysis.

3.2.1 SESTR-SESTR K^0_S Signal

The SESTR-SESTR K^0_S candidates are reconstructed from the two prong vertices in the vertex list. Figure 3.5 shows a $\pi\pi$ invariant mass histogram from SESTR-SESTR K^0_S candidates. The results in this histogram are from a single unfiltered raw data tape which had a total of about 800,000 events. The histogram is fitted with a gaussian signal and a linear background. From the fit I obtained the σ of the gaussian as 3.9 ± 0.1 MeV and the total number of entries in the gaussian signal as 4812 ± 80 events.

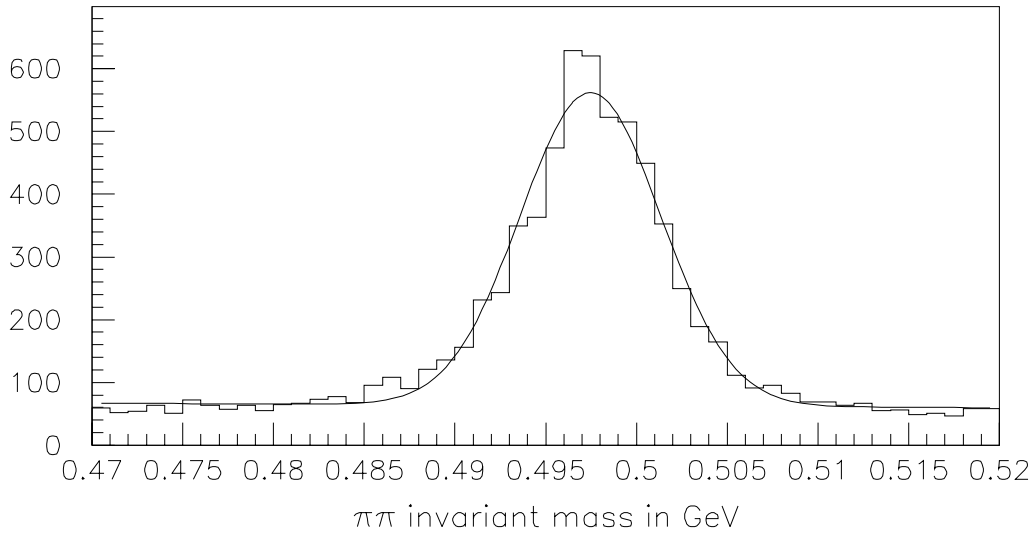

Figure 3.5: SESTR-SESTR K_S^0 signal from a single unfiltered DST tape. The K_S^0 candidates are required to have a SDZ > 15. The histogram is fitted with a gaussian signal and a linear background. From the fit I obtained the σ of the gaussian as 3.9 ± 0.1 MeV and the total number of entries in the signal as 4812 ± 80 events.

3.2.2 ESTR-ESTR K_s^0 Signal

The reconstruction package did not produce an ESTR-ESTR vertex list equivalent to the SESTR-SESTR vertex list. Therefore, ESTR-ESTR two prong vertices had to be reconstructed during stripping and analysis. Two prong vertices used for the ESTR-ESTR K_S^0 candidates were formed from oppositely charged tracks with χ^2 per degree of freedom less than 5. Additionally, only the category 3, 7, and 15 tracks were used; category 3,3 track combinations were not allowed. Once a vertex was formed the distance of closest approach (DCA) of the two tracks was required to be less than 0.5 cm. Figure 3.6 shows a $\pi\pi$ invariant mass histogram from ESTR-ESTR K_S^0 candidates. The results in this histogram are from a single unfiltered raw data tape which had a total of about 800,000 events. The histogram is fitted with a gaussian signal and a linear background. From the fit I obtained the σ of the gaussian as

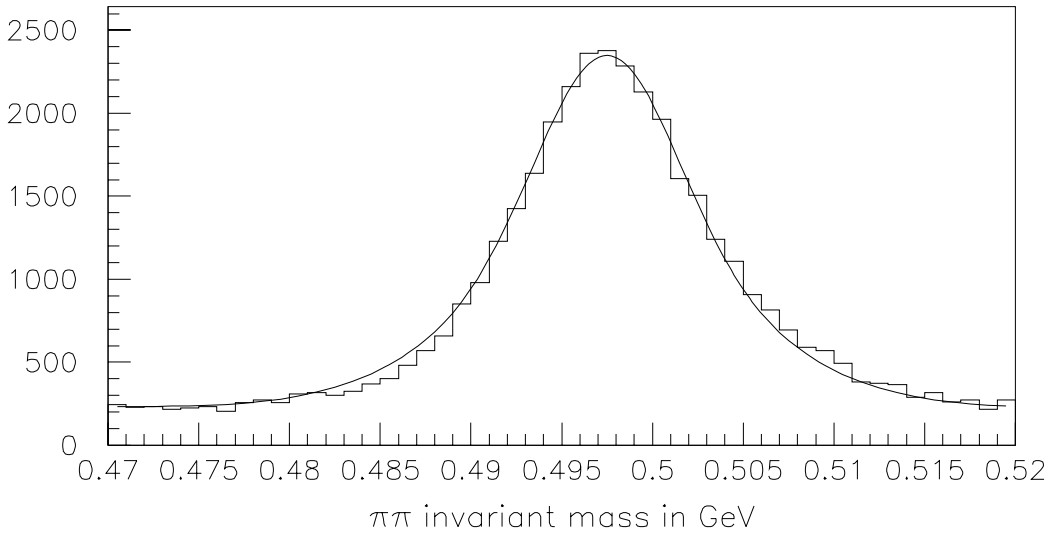

Figure 3.6: ESTR-ESTR K^0_S signal from a single unfiltered DST tape. The K^0_S candidates were required to have a DCA $< 0.5\,$cm. The histogram is fitted with a gaussian signal and a linear background. From the fit I obtained the σ of the gaussian as 5.8 ± 0.4 MeV and the total number of entries in the signal as 28433 ± 201 events.

5.8 ± 0.4 MeV and the total number of entries in the gaussian signal as 28433 ± 201 events.

3.2.2.1 DIP of ESTR-ESTR K^0_S candidates

Given the resolution of the drift chambers, the production and the decay vertices of short lived particles, such as D^0 candidates were indistinguishable to ESTR tracks. Therefore, with essentially no loss of signal we can reduce the background substantially by requiring the ESTR-ESTR K^0_S candidates point back to the primary vertex within a reasonable distance. Figure 3.7 shows the distribution of DIP of the ESTR-ESTR K^0_S candidates with respect to the primary vertex. The lighter region shows the DIP distribution for the background subtracted signal and the darker region shows that for the background. For the analysis presented in this thesis a DIP cut of 0.7cm

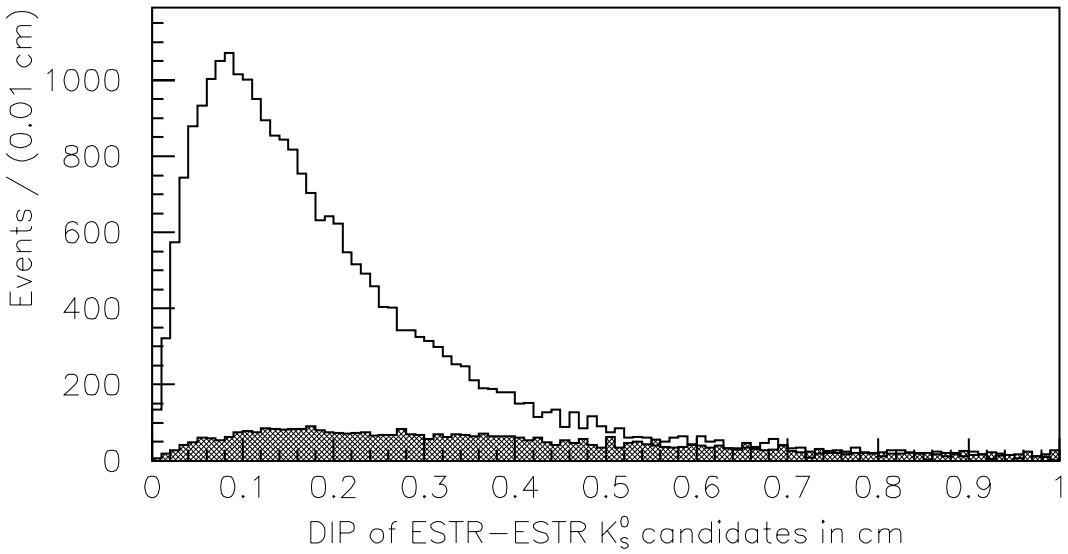

Figure 3.7: Distribution of DIP of the ESTR-ESTR K_S^0 candidates with respect to the primary vertex. The lighter region shows the DIP distribution for the background subtracted signal and the darker region shows that for the background.

was used to select the ESTR-ESTR K_S^0 candidates.

3.2.3 K_S^0 Mass Constraint Technique

Whenever I calculate the invariant mass of a parent particle which has a K_S^0 as a daughter, I constrain the mass of the daughter K_S^0 to be 497.6 MeV. First I calculate the momentum of the K_S^0 candidate from the two pion tracks which form the K_S^0. Then I assume that there is only a single particle with mass 497.6 MeV and the momentum given by the above estimation. This technique improved the mass resolution of the D^0 candidates by about 0.5 MeV compared to the nominal width of about 11 MeV.

3.3 Particle Identification Probabilities

From the knowledge, or the lack thereof, of the production rates of electrons, muons, pions, kaons and protons in experiments similar to E791, we have estimated the *a priori* probability for a track to be a electron, a muon, a pion, a kaon or a proton. These *a priori* probabilities are listed in Table 3.1. At the event reconstruction time *a priori* probabilities are changed to reflect the particle identification information from Čerenkov counters, calorimeters, and muon detectors. The exact values of the these probabilities are unimportant, because I am using them only as a figure of merit to find the amount of information available about the identity of the tracks.

Particle type	*a priori* probability
electron	0.02
muon	0.01
pion	0.81
kaon	0.12
proton	0.04

Table 3.1: Assumed *a priori* probabilities for electrons, muons, pions, kaons and protons

3.4 Filtering

In the release 5 version of the E791 filter code there were no special routines to select the candidates for the decays $D^0 \to K^0_S K\pi$ and $D^0 \to K^0_S \pi\pi$. Therefore, the events used in this analysis had to pass at least one of the following selection criteria in the release 5 filter:

1. SESTR-SESTR two prong vertex selection or

   - At least one two prong vertex with SDZ greater than 6.0 be in the vertex list.

2. ESTR-ESTR K^0_S selection.

   - At least one K^0_S candidate found using the criteria discussed in section 3.2.

3.5 Stripping $D^0 \to K^0_S K\pi$ and $D^0 \to K^0_S \pi\pi$ Candidates

At the stripping stage, we separated the events with $D^0 \to K^0_S K\pi$ and $D^0 \to K^0_S \pi\pi$ candidates using the criteria described later in this section. The cuts used at this stage were intended to be loose but sufficiently tight to give a finite size data sample after stripping; this would also allow us to study the optimal cuts later. As explained in section 2.4, the vertex reconstruction algorithm used in E791 was only 16% efficient in reconstructing $K\pi/\pi\pi$ vertices. To cope with this inefficiency, a candidate driven algorithm was used with the stripping code to reconstruct additional two prong $K\pi/\pi\pi$ vertices *(candidate driven method)*; details of which are given in appendix D.

Since, I compare the decays $D^0 \to K^0_S K\pi$ and $D^0 \to K^0_S \pi\pi$, candidates for both decays were selected with identical criteria except for the Čerenkov identification requirements used for $D^0 \to K^0_S K\pi$ candidates. In the first phase of stripping, all the K^0_S candidates were reconstructed as described in the section 3.2 and a list of K^0_Ss was formed. Then each candidate in the K^0_S list was combined with each two prong vertex from the vertex list as well as from the candidate driven method to form a three prong vertex. The two prong vertices were required to have minimum SDZ of 6. No duplicate tracks were allowed in this three prong vertex. Once the three track vertex was formed, then the DIP of the parent particle with respect to the primary vertex was calculated and it was required to be less than 80 μm. If the three track vertex passed all these requirements, then it was considered a possible D^0 vertex candidate.

At this point the Čerenkov identification probabilities of the two tracks that do

not come from the K^0_S were checked to identify possible candidates for the decay $D^0 \to K^0_S K\pi$. For D^0 candidate to qualify for the decay $D^0 \to K^0_S K\pi$, at least one of the two tracks in the $K\pi/\pi\pi$ vertex was required to have a kaon Čerenkov probability greater than 0.13. If only one of the tracks has a kaon Čerenkov probability greater than 0.13 then that track is identified as the kaon. If both tracks pass the minimum kaon Čerenkov probability cut then the product probability of one track being a kaon and the other being a pion is calculated. The kaon track is identified by the combination that gives the highest product probability.

Irrespective of the candidacy for the decay $D^0 \to K^0_S K\pi$, all D^0 candidates were considered as candidates for the decay $D^0 \to K^0_S\pi\pi$, and the $K^0_S K\pi$ and $K^0_S\pi\pi$ invariant masses were calculated as appropriate. Only candidates with the D^0 invariant mass between 1.7 GeV and 2.0 GeV were kept. The D^0 candidates were then combined with every SESTR track not already in the D^0 candidate vertex and with a χ^2/ν less than 5; to form $D^{*\pm}$ candidates. $D^{*\pm}$ candidates were required to have a D^*-D^0 mass difference within 4.0 MeV of 145.44 MeV. About 80% of the D^0 candidates were not consistent with coming from $D^{*\pm}$ candidates. Therefore, to suppress the large amounts of background being selected, tighter SDZ requirements were used for D^0 candidates not coming from D^* candidates compared to those coming from D^* candidates. Finally, the event was selected if at least one of the following criteria was satisfied:

- At least one D^0 candidate with a minimum SDZ of 6 and consistent with coming from a D^* candidate, or
- At least one D^0 candidate with a minimum SDZ of 8.

Chapter 4

The Analysis of the Decays $D^0 \to K^0_S K^{\pm}\pi^{\mp}$

In this analysis I study the sub-structure of $D^0 \to K^0_S K\pi$ and compare it with the decay $D^0 \to K^0_S\pi\pi$. The topological similarities of the decays $D^0 \to K^0_S K\pi$ and $D^0 \to K^0_S\pi\pi$ makes the decay $D^0 \to K^0_S\pi\pi$ particularly useful as a normalization mode. I have used Monte Carlo to correct for the differences in acceptance and reconstruction efficiency among different amplitudes of the decays $D^0 \to K^0_S K\pi$ and the decay $D^0 \to K^0_S\pi\pi$. The Čerenkov efficiency for identifying kaons in selecting $D^0 \to K^0_S K\pi$ candidates was determined from data using $D^+ \to K^-\pi^+\pi^+$ signals. The details of these efficiency studies are given in Appendix B. The charge conjugate modes are implicitly included in this analysis.

4.1 Final Event Selection

Very little Čerenkov information is available for momenta less than 6 GeV or greater than 60 GeV. Therefore, to compare the decays $D^0 \to K^0_S\pi\pi$ and $D^0 \to K^0_S K\pi$, the

momenta of the two tracks that do not come from the K^0_S were required to be between 6 GeV and 60 GeV and the momenta of the D^0 candidates were required to be 30 GeV or more. The topological cuts were obtained by tuning on the $D^{*+} \to D^0\pi^+$, $D^0 \to K^0_S\pi\pi$ signal from 80 runs (about 2.5 billion events) of data, which constitute 45% of my final data sample.

Following is a complete list of the cuts used to select the final data sample:

1. D^0 candidates with the secondary vertex in a target foil were explicitly excluded as are all candidates downstream of the interaction counter,

2. The D^0 candidates were required to have a minimum momentum of 30.0 GeV,

3. The momenta of each of the tracks that do not come from the K^0_S were required to be between 6 GeV and 60 GeV,

4. The SESTR-SESTR K^0_S candidates were required to have a minimum SDZ of 15,

5. ESTR-ESTR K^0_S candidates were allowed to have a maximum DCA of 0.5 cm with the decay vertex downstream of 10 cm. Also a the DIP of the ESTR-ESTR K^0_S candidates with respect to the primary vertex was required to be less than 0.7 cm,

6. The K^0_S mass is restricted to lie between 485.0 MeV and 509.0 MeV,

7. If the $K\pi/\pi\pi$ vertex was found from the vertex list and the K^0_S candidate is from ESTR tracks, then the $K\pi/\pi\pi$ vertex was required to have a minimum SDZ of 13 and the D^0 candidate was allowed to have a maximum DIP of 50 μm with respect to the primary vertex,

8. If the $K\pi/\pi\pi$ vertex was found from the vertex list and the K^0_S candidate is from SESTR tracks, then the $K\pi/\pi\pi$ vertex was required to have a minimum

SDZ of 10 and the D^0 candidate was allowed to have a maximum DIP of 50 μm with respect to the primary vertex,

9. If the $K\pi/\pi\pi$ vertex was found from the candidate driven method and the K^0_S candidate is from ESTR tracks, then the $K\pi/\pi\pi$ vertex was required to have a SDZ between 10 and 20 and the D^0 candidate was allowed to have a maximum DIP of 20 μm with respect to the primary vertex,

10. If the $K\pi/\pi\pi$ vertex was found from the candidate driven method and the K^0_S candidate is from SESTR tracks, then the $K\pi/\pi\pi$ vertex was required to have a SDZ between 10 and 20 and the D^0 candidate was allowed to have a maximum DIP of 30 μm with respect to the primary vertex,

11. The kaon Čerenkov probability of the kaon in the $K^0_S K\pi$ candidates is required to be greater than 0.15,

12. The mass of the D^0 candidates are required to be between 1.7 GeV and 2.0 GeV, and

13. D^0 candidates are considered consistent with originating from the decay $D^{*+} \rightarrow D^0\pi^+$, if a D^* is found with the D^*-D^0 mass difference within 1.5 MeV of 145.44 MeV.

4.2 Division of the Signals into Sub-Samples

About 17% of the D^0 signals found was consistent with originating from the decay $D^{*+} \rightarrow D^0\pi^+$. The D^0 signal from events that do not come from the decay $D^{*+} \rightarrow D^0\pi^+$ has a larger background but a better statistical significance[1] compared to the

[1]Fourteen sigma compared to ten sigma in the case of $D^0 \rightarrow K^0_S\pi\pi$

signal from the ones that come from D^* decays. When the D^0 candidates are not coming from D^{*+} decays we cannot separate the two channels $D^0 \to K^0_S K^+\pi^-$ and $D^0 \to K^0_S K^-\pi^+$, but we can use the combined signals to constrain the fits, especially in the decays which are not observed. Therefore, to take the advantage of this non D^* signal to study the sub-structure of the decay $D^0 \to K^0_S K\pi$, I divided my data sample into eleven sub-samples as described in this section.

The events consistent with the decay $D^0 \to K^0_S K\pi$ were first separated into three mutually exclusive categories I, II and III in that order.

(I) Candidates for the resonant decays $K^{*+}K^-$ or K^+K^{*-}

(II) Candidates for the resonant decays $\overline{K}^{*0}K^0$ or $K^{*0}\overline{K}^0$

(III) Candidates for the non-resonant decays $K^0_S K^-\pi^+$ or $K^0_S K^+\pi^-$

The K^* candidates were required to pass the following two cuts:

- The mass of the K^* candidate should be within 40 MeV of 892 MeV, and
- $|\cos\theta| > 0.3$, where θ is the polar angle of the π in the K^* center of mass frame and $\theta = 0$ is the direction of the K^* in the $K^0_S K\pi$ center of mass frame[2].

The events in each of the above three categories I, II and III were again sub-divided into two groups depending on whether they are consistent with coming from the decay $D^{*+} \to D^0\pi^+$ or not. Finally, the events coming from D^{*+} decays were further separated into two groups according to the candidacy for the decays $D^0 \to$

[2] $D^0 \to K^*K$ is a pseudoscalar $\to$ vector + pseudoscalar decay with an angular distribution of $dN/d\cos\theta \propto \cos^2\theta$

<table>
<tr><td colspan="6">$K^0_S K\pi$ Candidates</td></tr>
<tr><td colspan="2">$K^{*+}K^-$ or $K^{*-}K^+$</td><td colspan="2">$\overline{K}^{*0}K^0$ or $K^{*0}\overline{K}^0$</td><td colspan="2">Non-Resonant</td></tr>
<tr><td colspan="2">From D^{*+}</td><td colspan="2">From D^{*+}</td><td colspan="2">From D^{*+}</td></tr>
<tr><td>(1)
$K^{*+}K^-$</td><td>(2)
$K^{*-}K^+$</td><td>(4)
$\overline{K}^{*0}K^0$</td><td>(5)
$K^{*0}\overline{K}^0$</td><td>(7)
$K^0_S K^-\pi^+$</td><td>(8)
$K^0_S K^+\pi^-$</td></tr>
<tr><td colspan="2">(3)
Not from D^{*+}
$K^{*+}K^-$ or $K^{*-}K^+$</td><td colspan="2">(6)
Not from D^{*+}
$\overline{K}^{*0}K^0$ or $K^{*0}\overline{K}^0$</td><td colspan="2">(9)
Not from D^{*+}
Non-Resonant</td></tr>
</table>

Table 4.1: The nine mutually exclusive samples sub-samples of $K^0_S K\pi$ candidates

<table>
<tr><td>$K^0_S\pi\pi$ Candidates</td></tr>
<tr><td>From the decay $D^{*+} \to D^0\pi^+$
(10)</td></tr>
<tr><td>Not from the decay $D^{*+} \to D^0\pi^+$
(11)</td></tr>
</table>

Table 4.2: The two mutually exclusive samples sub-samples of $K^0_S\pi\pi$ candidates

$K^0_S K^-\pi^+$ and $D^0 \to K^0_S K^+\pi^-$. The $D^0 \to K^0_S\pi\pi$ candidates were also divided into two mutually exclusive samples according to the D^{*+} hypothesis.

4.3 Maximum Likelihood Fit

To extract the signals of interest from the eleven sub-samples, I fit the data with a single 32 parameter maximum likelihood fit. This section describes the maximum likelihood fit in three parts: modeling the data, formalizing the likelihood function, and evaluating the likelihood function.

4.3.1 Modeling the Data Set

The first step in a maximum likelihood fit is to find a set of parameters to model the data. In this analysis I model each of the 11 sub-samples described in section 4.2 by a gaussian signal plus a linear background. Background in each of the sub-samples is represented by two parameters, intercept and slope, which gives 22 parameters altogether. The following ten parameters describe the signals in my data set.

- T_1 - Total observed signal from the decay $D^0 \to K^0_S\pi\pi$
- T_2, T_3,....,T_7 - Total observed $K^0_SK\pi$ signal events from the decays $K^{*+}K^-$, $K^{*-}K^+$, $\overline{K}^{*0}K^0$, $K^{*0}\overline{K}^0$, non-resonant $K^0_SK^-\pi^+$ and $K^0_SK^+\pi^-$ respectively, corrected for the relative inefficiencies[3] of $D^0 \to K^0_SK\pi$ and $D^0 \to K^0_S\pi\pi$ decay modes and the fraction of K^*s decaying to charged pions.
- f_{D^*} - Fraction of the observed signals coming from $D^{*+} \to D^0\pi^+$ decays. This fraction is assumed to be the same for $D^0 \to K^0_SK\pi$ and $D^0 \to K^0_S\pi\pi$ decays.
- M_{D^0} - Mass of the D^0 candidates
- σ - Gaussian width of the $D^0 \to K^0_S\pi\pi$ signal.

[3] $D^0 \to K^0_S\pi\pi$ efficiency is taken to be 100% and T_2 through T_7 are corrected accordingly (see appendix B).

I use the following formula to relate the widths of the gaussian signals from $D^0 \to K^0_S K\pi$ and $D^0 \to K^0_S \pi\pi$ (see Appendix C.1).

$$\sigma_{K^0_S K\pi} = \sigma_{K^0_S \pi\pi} \; - \; 1.1\,\mathrm{MeV}$$

4.3.2 The Likelihood Function

For each sub-sample described in section 4.2 we can write a likelihood function as

$$\mathcal{L} = \left\{ \frac{e^{-\nu}\nu^n}{n!} \right\} \mathrm{x} \prod_{\mathrm{i}=1}^{\mathrm{n}} \mathrm{P_i}$$

where n is the total number of observed events in the sub-sample, ν is the number of events predicted to be in the sub-sample, and $\mathrm{P_i}$ is the probability of observing an event in this sub-sample at the mass of the i^{th} candidate. $\mathrm{P_i}$ and ν are functions of the 32 parameters described in the section 4.3.1. Once the likelihood functions for all the sub-samples are written, the goal is to find a set values for the 32 parameters that will simultaneously maximize all the likelihood functions. In this analysis we achieve this goal by maximizing the logarithm of the product of the eleven likelihood functions.

4.3.3 Estimation of $\mathrm{P_i}$ and ν

The probability of observing a given event depends on the expected total signal and the background of the sub-sample in which the event appears. The predicted total signal in each of the sub-samples is estimated from the signal parameters $\mathrm{T}_1, \ldots, \mathrm{T}_7$, the fraction of the total events coming from D^* decays, f_{D^*}, and the relative efficiencies ϵ_{ij} for observing the decay $D^0 \to K^0_S K\pi$. Since I am comparing the $D^0 \to K^0_S K\pi$ decays with $D^0 \to K^0_S \pi\pi$ decays, the ϵ_{ij} coefficients are calculated with respect to the

decay $D^0 \to K^0_S\pi\pi$. A detailed description of the ϵ_{ij} coefficients are given in appendix B. To exclude the reflection of the $K^0_S\pi\pi$ signal in the $K^0_S K\pi$ invariant mass plots, I use only the events in the mass range 1.7 GeV to 1.95 GeV for the $K^0_S K\pi$ sub-samples (see Appendix C.2). The total predicted signal in each of the eleven sub-samples[4] is calculated as follows.

- Sub-Sample 1: ($K^{*+}K^-$ events originating from D^{*+} decays)

  Predicted total signal = $\mathrm{T}_2 * \mathrm{f}_{\mathrm{D}^*} * \epsilon_{11} + \mathrm{T}_4 * \mathrm{f}_{\mathrm{D}^*} * \epsilon_{12} + \mathrm{T}_6 * \mathrm{f}_{\mathrm{D}^*} * \epsilon_{13}$

- Sub-Sample 2: ($K^{*-}K^+$ events originating from D^{*+} decays)

  Predicted total signal = $\mathrm{T}_3 * \mathrm{f}_{\mathrm{D}^*} * \epsilon_{11} + \mathrm{T}_5 * \mathrm{f}_{\mathrm{D}^*} * \epsilon_{12} + \mathrm{T}_7 * \mathrm{f}_{\mathrm{D}^*} * \epsilon_{13}$

- Sub-Sample 3: ($K^{*+}K^-$ and $K^{*-}K^+$ events not originating from D^{*+} decays)

  Predicted total signal = $(\mathrm{T}_2 + \mathrm{T}_3) * (1 - \mathrm{f}_{\mathrm{D}^*}) * \epsilon_{11} +$
  $(\mathrm{T}_4 + \mathrm{T}_5) * (1 - \mathrm{f}_{\mathrm{D}^*}) * \epsilon_{12} +$
  $(\mathrm{T}_6 + \mathrm{T}_7) * (1 - \mathrm{f}_{\mathrm{D}^*}) * \epsilon_{13}$

- Sub-Sample 4: ($\overline{K}^{*0}K^0$ events originating from D^{*+} decays)

  Predicted total signal = $\mathrm{T}_2 * \mathrm{f}_{\mathrm{D}^*} * \epsilon_{21} + \mathrm{T}_4 * \mathrm{f}_{\mathrm{D}^*} * \epsilon_{22} + \mathrm{T}_6 * \mathrm{f}_{\mathrm{D}^*} * \epsilon_{23}$

- Sub-Sample 5: ($K^{*0}\overline{K}^0$ events originating from D^{*+} decays)

  Predicted total signal = $\mathrm{T}_3 * \mathrm{f}_{\mathrm{D}^*} * \epsilon_{21} + \mathrm{T}_5 * \mathrm{f}_{\mathrm{D}^*} * \epsilon_{22} + \mathrm{T}_7 * \mathrm{f}_{\mathrm{D}^*} * \epsilon_{23}$

[4]The division of the samples is explained in section 4.2

- Sub-Sample 6: ($\overline{K}^{*0}K^0$ and $K^{*0}\overline{K}^0$ events not originating from D^{*+} decays)

  Predicted total signal = $(\mathrm{T}_2 + \mathrm{T}_3) * (1 - \mathrm{f}_{\mathrm{D}^*}) * \epsilon_{21}$ +
  $(\mathrm{T}_4 + \mathrm{T}_5) * (1 - \mathrm{f}_{\mathrm{D}^*}) * \epsilon_{22}$+
  $(\mathrm{T}_6 + \mathrm{T}_7) * (1 - \mathrm{f}_{\mathrm{D}^*}) * \epsilon_{23}$

- Sub-Sample 7: (Non-resonant $K^0_S K^-\pi^+$ events originating from D^{*+} decays)

  Predicted total signal = $\mathrm{T}_2 * \mathrm{f}_{\mathrm{D}^*} * \epsilon_{31} + \mathrm{T}_4 * \mathrm{f}_{\mathrm{D}^*} * \epsilon_{32} + \mathrm{T}_6 * \mathrm{f}_{\mathrm{D}^*} * \epsilon_{33}$

- Sub-Sample 8: (Non-resonant $K^0_S K^+\pi^-$ events originating from D^{*+} decays)

  Predicted total signal = $\mathrm{T}_3 * \mathrm{f}_{\mathrm{D}^*} * \epsilon_{31} + \mathrm{T}_5 * \mathrm{f}_{\mathrm{D}^*} * \epsilon_{32} + \mathrm{T}_7 * \mathrm{f}_{\mathrm{D}^*} * \epsilon_{33}$

- Sub-Sample 9: (Non-resonant $K^0_S K^-\pi^+$ and $K^0_S K^+\pi^-$ events not originating from D^{*+} decays)

  Predicted total signal = $(\mathrm{T}_2 + \mathrm{T}_3) * (1 - \mathrm{f}_{\mathrm{D}^*}) * \epsilon_{31}$ +
  $(\mathrm{T}_4 + \mathrm{T}_5) * (1 - \mathrm{f}_{\mathrm{D}^*}) * \epsilon_{32}$ +
  $(\mathrm{T}_6 + \mathrm{T}_7) * (1 - \mathrm{f}_{\mathrm{D}^*}) * \epsilon_{33}$

- Sub-Sample 10: ($K^0_S\pi^+\pi-$ events originating from D^{*+} decays)

  Predicted total signal = $\mathrm{T}_1 * \mathrm{f}_{\mathrm{D}^*}$

- Sub-Sample 11: ($K^0_S\pi^+\pi-$ events not originating from D^{*+} decays)

  Predicted total signal = $\mathrm{T}_1 * (1 - \mathrm{f}_{\mathrm{D}^*})$

For the i$^{\text{th}}$ candidate in a given sub-sample, the amount of expected signal and background at the invariant mass of that candidate (m_i) is given by

$$\text{Signal}_\text{i} = \text{Predicted\_total\_signal} * \frac{1}{\sqrt{2\pi}\sigma} * \text{e}^{-\left\{ \frac{1}{2} \left(\frac{\text{M}_{D^0} - \text{m}_\text{i}}{\sigma} \right)^2 \right\}}$$

$$\text{Background}_\text{i} = A + B * m_i$$

where A and B are the intercept and the slope of the fitted linear background. The total predicted background in the sub-sample is obtained by integrating the background over the mass range of the sub-sample. Due to the different mass ranges[5] used for the $K^0_S K\pi$ and $K^0_S \pi\pi$ sub-samples, the predicted total backgrounds are different for the two decays and are given by

- For $K^0_S K\pi$ decays

  Predicted total background $= \int_{1.7}^{1.95} (A + B * m) dm = 0.25 * A + 0.456 * B$
- For $K^0_S \pi\pi$ decays

  Predicted total background $= \int_{1.7}^{2.0} (A + B * m) dm = 0.25 * A + 0.555 * B$

Then P_i and ν can be written as

$$\nu = \text{Predicted\_total\_signal} + \text{Predicted\_total\_background}$$

$$\text{P}_\text{i} = (\text{Signal}_\text{i} + \text{Background}_\text{i})/\nu$$

[5] 1.7 GeV to 1.95 GeV for $K^0_S K\pi$ decays and 1.7 GeV to 2.0 GeV for the $K^0_S \pi\pi$ decays (see appendix C.2)

4.4 Results from the Maximum Likelihood Fit

From my analysis, I have observed 75±16 $K^0_S K\pi$ signal events in the decay $D^0 \to K^{*-}K^+$ and 960 ± 64 signal events in the decay $D^0 \to K^0_S\pi\pi$. These numbers are not corrected for the observation inefficiencies and the errors are statistical only. The observed signals in all the other decays were consistent with being zero. The amount of observed events corrected for the inefficiencies[6] of the $K^0_S K\pi$ decays with respect to $K^0_S\pi\pi$ decays, as found from the found from the maximum likelihood fit, are listed in Table 4.3. 90% confidence level upper limits are reported for the decays without clear signals. Please see appendix F for details on calculating these 90% confidence level upper limits.

Decay mode	Amount of observed events
$K^0_S\pi^+\pi^-$	960 ± 64
$K^{*+}K^-$	198 ± 41
$K^{*-}K^+$	< 66
$\overline{K}^{*0}K^0$	< 102
$K^{*0}\overline{K}^0$	< 80
$K^0_S K^-\pi^+$ (non-resonant)	< 46
$K^0_S K^+\pi^-$ (non-resonant)	< 45

Table 4.3: The amount of observed events corrected for the relative inefficiencies of the $K^0_S K\pi$ decays with respect to $K^0_S\pi\pi$ decays. 90% confidence level upper limits are reported for the decays without clear signals. The errors are statistical only.

Figures 4.1 through 4.11 show the final D^0 mass histograms from my analysis. The solid curves are the projections from the maximum likelihood fit. In the maximum likelihood fit, I allow for the feedthrough of different $K^0_S K\pi$ decays, through the efficiency matrix ϵ_{ij} (see appendix B.1). As a result of this, the projections from the maximum likelihood fit shows signals in the $K^{*-}K^+$, $\overline{K}^{*0}K^0$, $K^{*0}\overline{K}^0$, and non-

[6] The details of the inefficiency corrections can be found in the appendix B.

resonant $K^0_S K^-\pi^+$ and $K^0_S K^+\pi^-$ decays even though no clear signals were observed in those decay modes. The dotted lines in the figures show the 90% confidence level upper limit projections. To obtain these 90% confidence level projections, I set the parameter in question to its 90% confidence level upper limit, then refit the data allowing the other parameters to float, and projected back the resulting curve onto the relevant histogram. From the maximum likelihood fit, I found the σ of the $K^0_S\pi\pi$ signal to be 11.3 $\pm$ 0.7 MeV and the fraction of the D^0 signals appearing as coming from D^* decays to be 0.17$\pm$0.02. The background parameters from the straight line fits to the histograms in Figures 4.1 through 4.11 are listed in Table 4.4.

Histogram	Intercept at 1.7 GeV	Intercept at 2.0 GeV
Figure 4.1	12$\pm$1	9$\pm$1
Figure 4.2	481$\pm$8	308$\pm$7
Figure 4.3	27$\pm$2	11$\pm$2
Figure 4.4	0.5$\pm$0.2	0.00$\pm$0.02
Figure 4.5	0.3$\pm$0.2	0.5$\pm$0.2
Figure 4.6	36$\pm$2	14$\pm$2
Figure 4.7	0.7$\pm$0.3	0.3$\pm$0.2
Figure 4.8	0.5$\pm$0.2	0.4$\pm$0.2
Figure 4.9	179$\pm$5	197$\pm$6
Figure 4.10	1.8$\pm$0.6	2.9$\pm$0.7
Figure 4.11	3.5$\pm$0.7	3.1$\pm$0.8

Table 4.4: Parameters of the straight line fits to the backgrounds of the histograms in Figures 4.1 through 4.11.

The relative and absolute branching ratios and 90% confidence level upper limits obtained from the maximum likelihood fit are reported in Table 4.5. The relative branching ratios are obtained by comparing with the decay $D^0 \to K^0_S\pi\pi$. The Particle Data Group branching ratio for the decay $D^0 \to \overline{K}^0\pi^+\pi^-$, (5.4$\pm$0.5)%, was used to obtain the absolute branching ratios. The errors reported are statistical and systematic respectively. The third error in the absolute branching ratio of $K^{*+}K^-$

is from the 11% error in the $D^0 \to \overline{K}^0\pi^+\pi^-$ branching ratio. The systematic errors were computed by varying the Čerenkov efficiency for identifying kaons, the difference between the widths of $K^0_S K\pi$ and $K^0_S\pi\pi$ signals and the relative observation efficiencies ϵ_{ij}. The major contributor to the systematic error was the relative observation efficiencies, ϵ_{ij}, calculated from Monte Carlo events. With a better understanding of the Monte Carlo data we should be able to reduce this systematic error to a 10% level.

D^0 decay mode	Relative branching ratio	Absolute branching ratio (%)
$K^{*+}K^-$	$0.21\pm0.04\pm0.03$	$1.1\ \pm0.2\pm0.2\pm0.1$
$K^{*-}K^+$	< 0.07	< 0.37
$\overline{K}^{*0}K^0$	< 0.11	< 0.57
$K^{*0}\overline{K}^0$	< 0.08	< 0.45
$K^0K^-\pi^+$ (non-resonant)	< 0.05	< 0.26
$\overline{K}^0K^+\pi^-$ (non-resonant)	< 0.05	< 0.25

Table 4.5: Relative and absolute branching ratios and 90% confidence level upper limits. Relative branching ratios are calculated by comparing with the decay $D^0 \to K^0_S\pi\pi$. The Particle Data Group branching ratio for the decay $D^0 \to \overline{K}^0\pi^+\pi^-$, $(5.4\pm0.5)\%$ was used to obtain the absolute branching ratios.

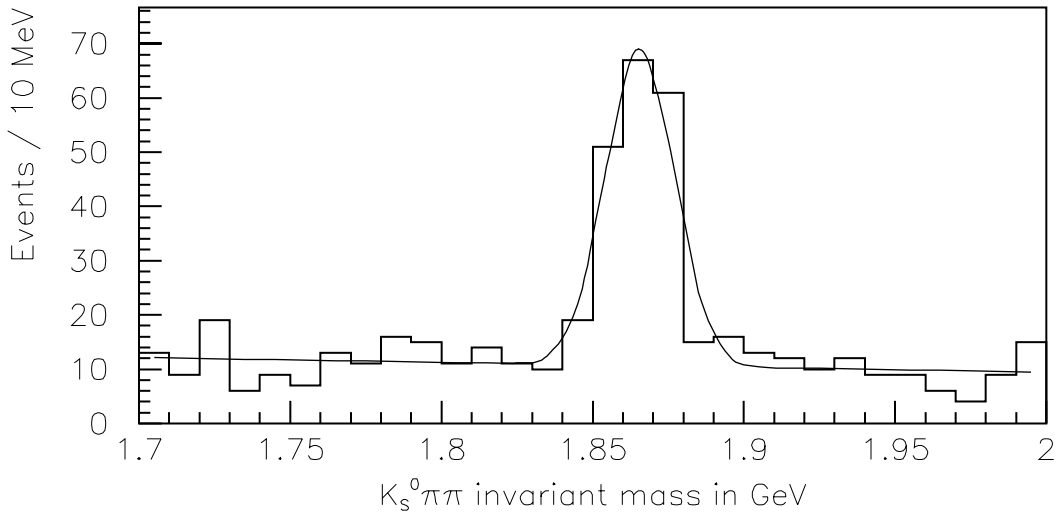

Figure 4.1: The $K^0_S\pi\pi$ invariant mass histogram from the decay $D^0 \to K^0_S\pi\pi$, for the events that are consistent with originating from the decay $D^{*+} \to D^0\pi^+$. The curve is the projection from the maximum likelihood fit. From the maximum likelihood fit I obtained the amount of signal as 166 ± 19 events.

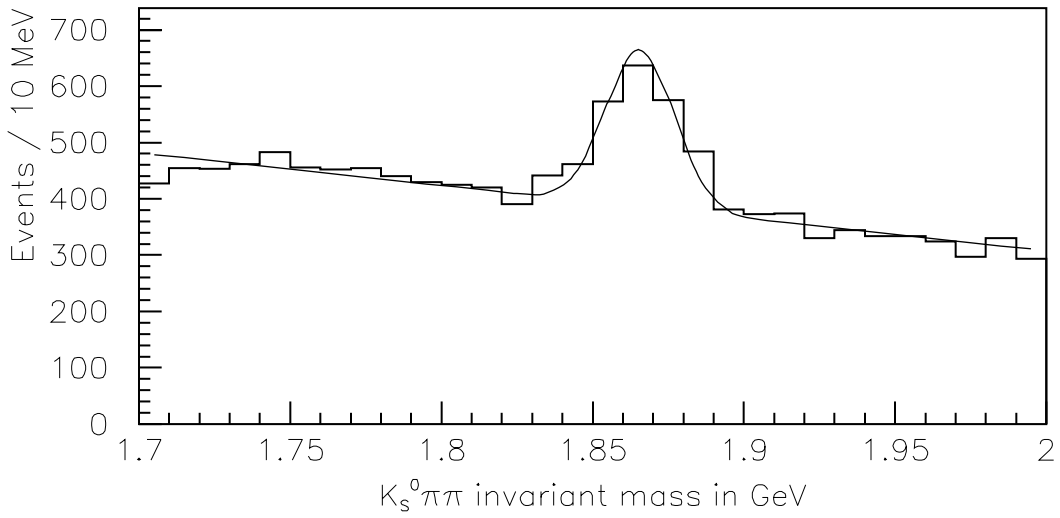

Figure 4.2: The $K^0_S\pi\pi$ invariant mass histogram from the decay $D^0 \to K^0_S\pi\pi$, for the events that are not consistent with originating from the decay $D^{*+} \to D^0\pi^+$. From the maximum likelihood fit I obtain the amount of signal as $794\pm$ 55 events.

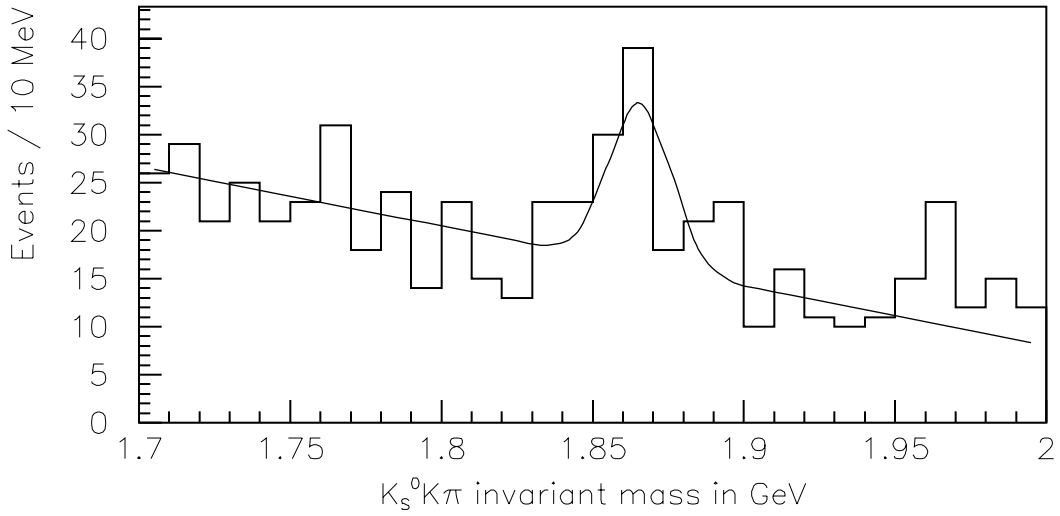

Figure 4.3: The $K^0_S K\pi$ invariant mass histogram from the events that are not consistent with the decay $D^{*+} \to D^0\pi^+$ but are consistent with one of the resonant decays $D^0 \to K^{*+}K^-$ or $D^0 \to K^{*-}K^+$. The curve is the projection from the maximum likelihood fit.

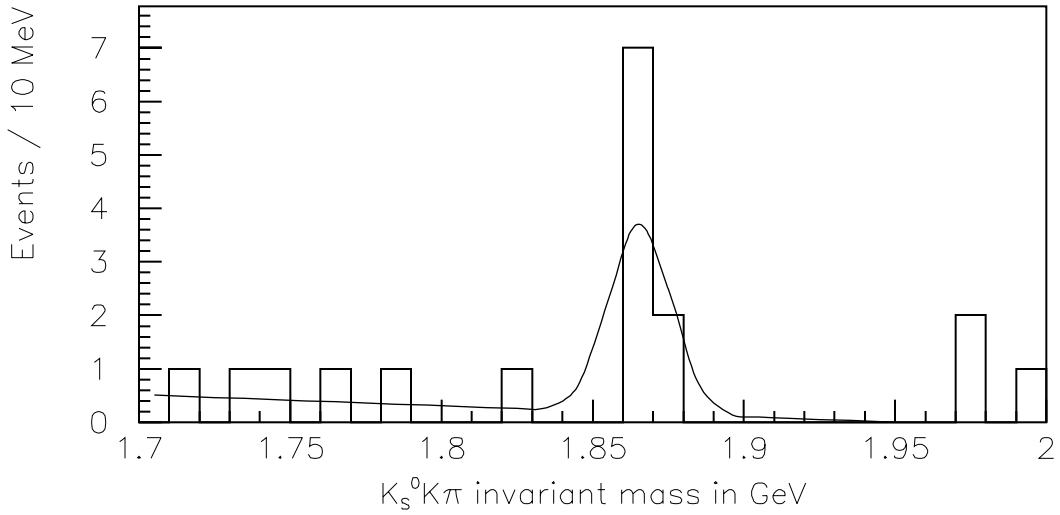

Figure 4.4: The $K^0_S K\pi$ invariant mass histogram from the events that are consistent with the decay $D^{*+} \to D^0\pi^+$ and $D^0 \to K^{*+}K^-$. The curve is the projection from the maximum likelihood fit.

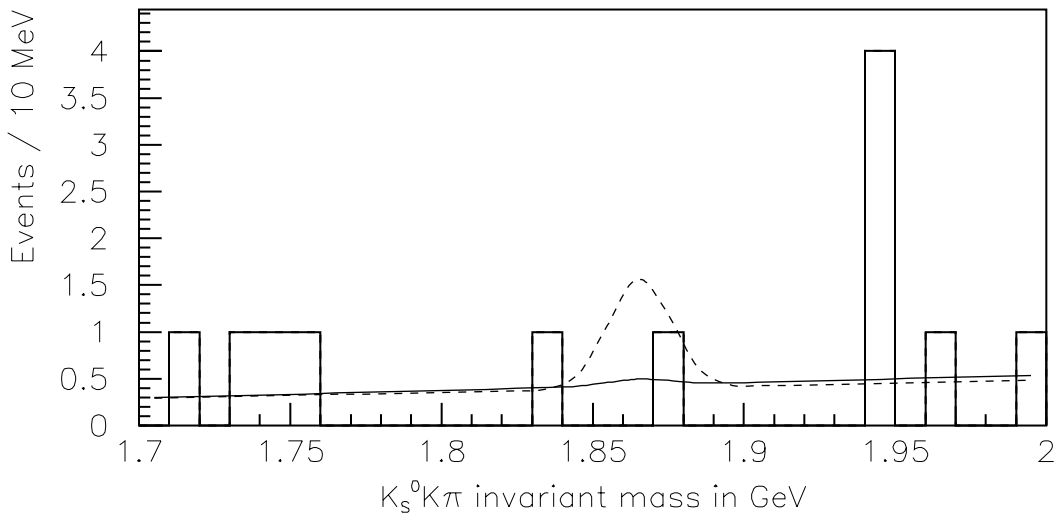

Figure 4.5: The $K^0_S K\pi$ invariant mass histogram from the events that are consistent with the decays $D^{*+} \to D^0\pi^+$ and $D^0 \to K^{*-}K^+$. The solid curve is the projection from the maximum likelihood fit and the dashed line is the 90% confidence level upper limit projection.

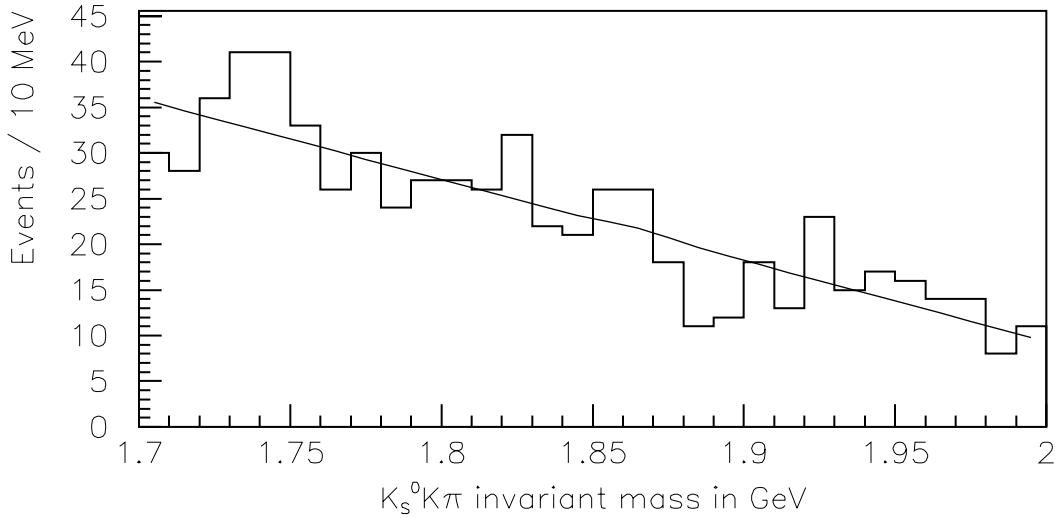

Figure 4.6: The $K^0_S K\pi$ invariant mass histogram from the events that are not consistent with the decay $D^{*+} \to D^0\pi^+$ but are consistent with one of the resonant decays $D^0 \to \overline{K}^{*0}K^0$ or $D^0 \to K^{*0}\overline{K}^0$. The curve is the projection from the maximum likelihood fit.

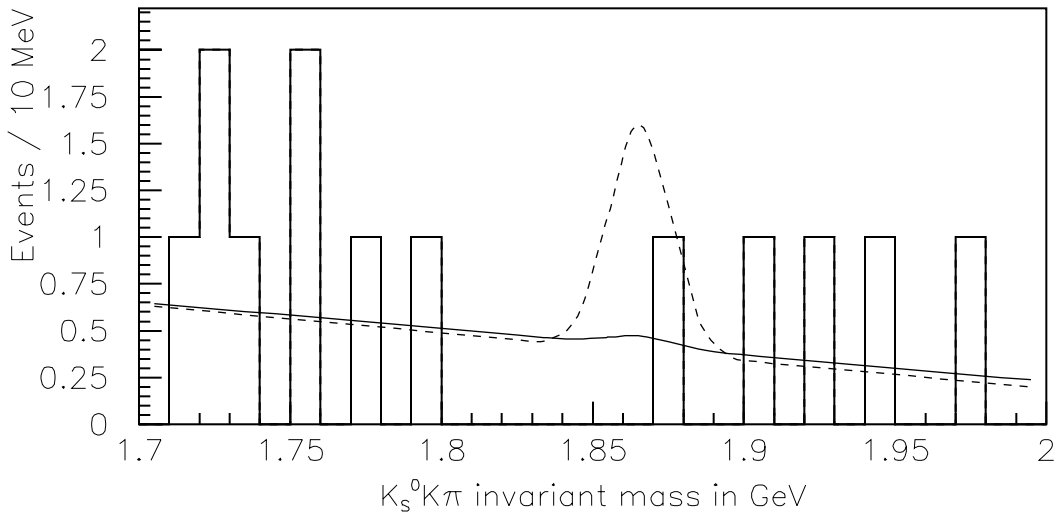

Figure 4.7: The final $K_S^0 K\pi$ invariant mass histogram from the events that are consistent with the decays $D^{*+} \to D^0\pi^+$ and $D^0 \to \overline{K}^{*0}K^0$. The solid curve is the projection from the maximum likelihood fit and the dashed curve is the 90% confidence level upper limit projection.

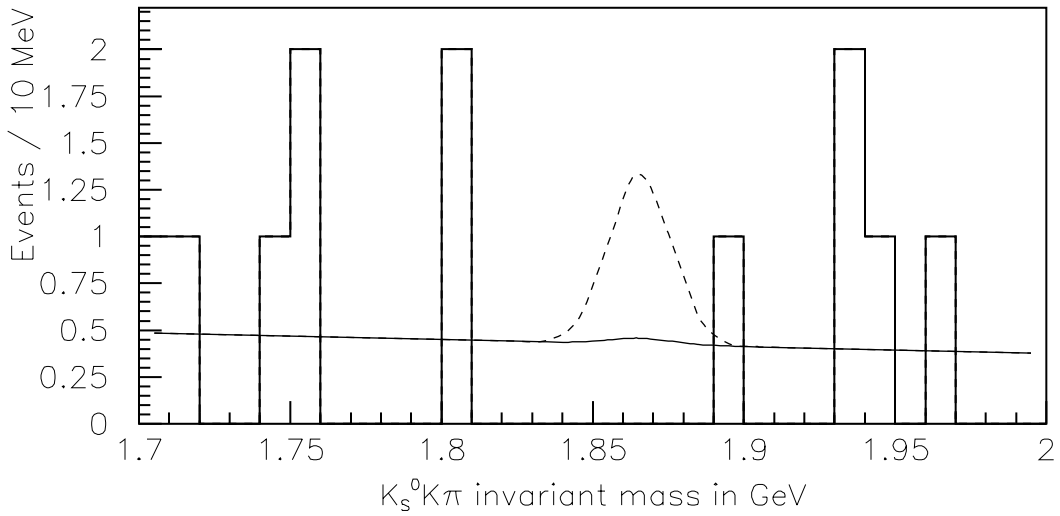

Figure 4.8: The final $K_S^0 K\pi$ invariant mass histogram from the events that are consistent with the decays $D^{*+} \to D^0\pi^+$ and $D^0 \to K^{*0}\overline{K}^0$. The solid curve is the projection from the maximum likelihood fit and the dashed curve is the 90% confidence level upper limit projection.

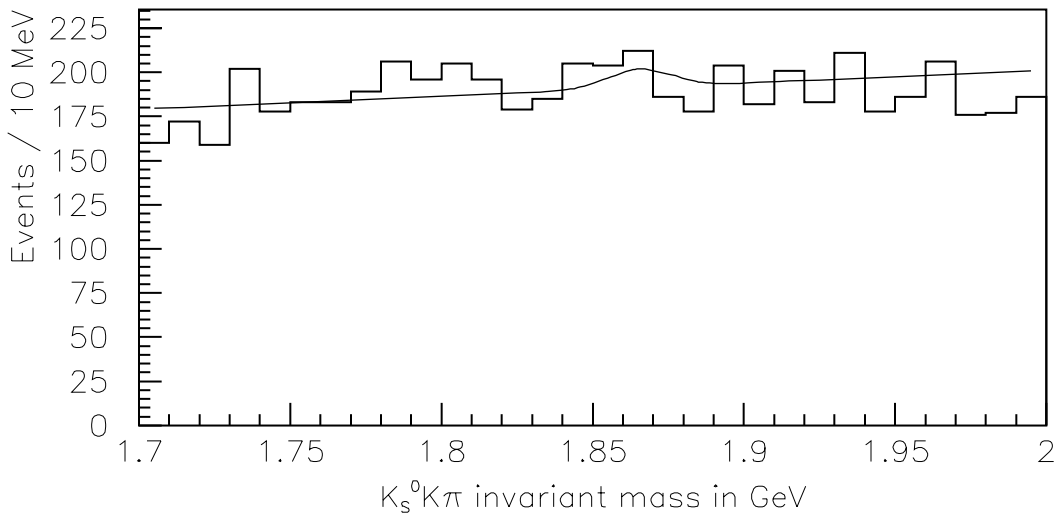

Figure 4.9: The final $K_S^0 K\pi$ invariant mass histogram from the events that are not consistent with the decay $D^{*+} \to D^0\pi^+$ but are consistent with one of the non-resonant decays $D^0 \to K^0K^-\pi^+$ or $D^0 \to \overline{K}^0K^+\pi^-$. The curve is the projection from the maximum likelihood fit.

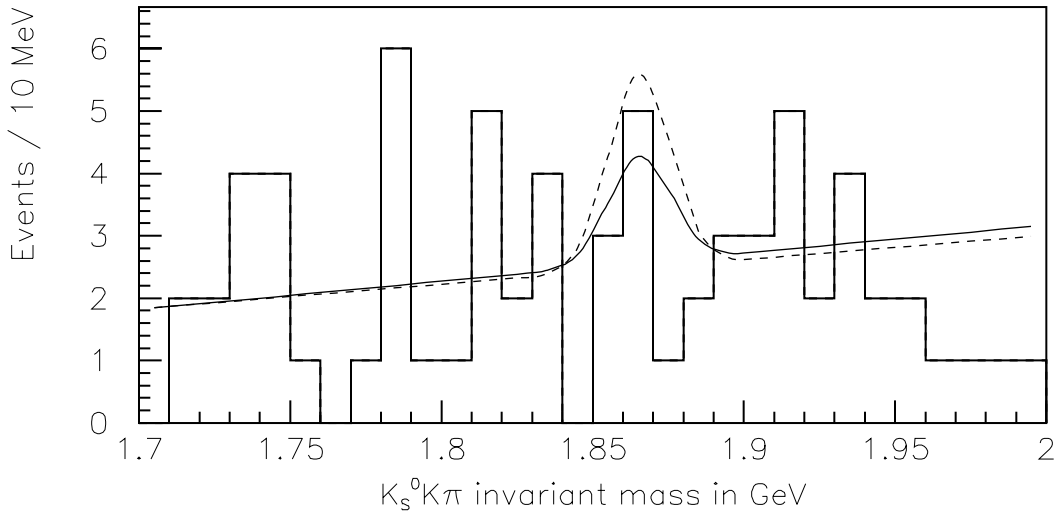

Figure 4.10: The final $K_S^0 K\pi$ invariant mass histogram from the events that are consistent with the decays $D^{*+} \to D^0\pi^+$ and $D^0 \to K^0K^-\pi^+$. The solid curve is the projection from the maximum likelihood fit and the dashed curve is the 90% confidence level upper limit projection.

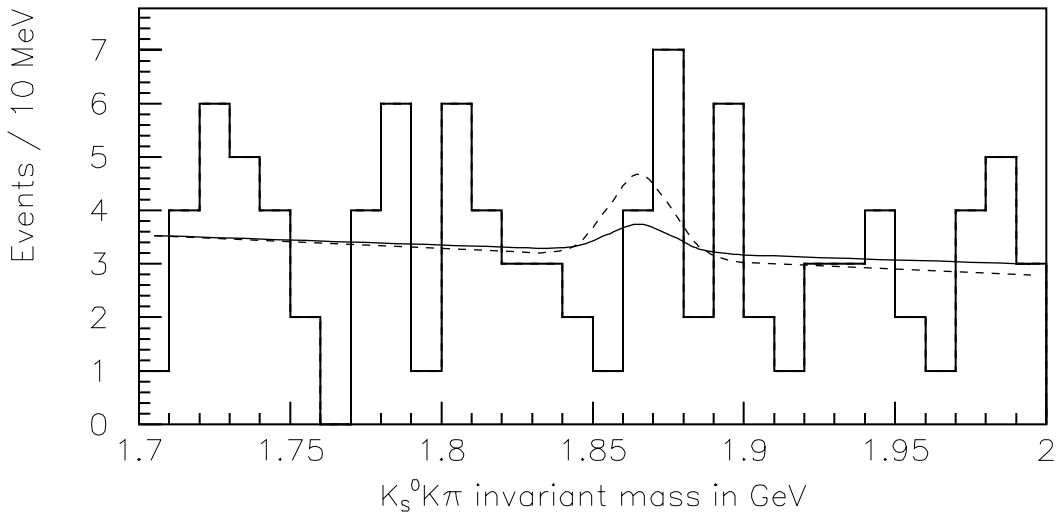

Figure 4.11: The final $K_S^0 K\pi$ invariant mass histogram from the events that are consistent with the decays $D^{*+} \to D^0\pi^+$ and $D^0 \to \overline{K}^0 K^+\pi^-$. The solid curve is the projection from the maximum likelihood fit and the dashed curve is the 90% confidence level upper limit projection.

Chapter 5

Results and the Conclusions

I have analyzed 30% of the full E791 data set and studied the decay $D^0 \to K^0_S K\pi$. The resonant sub-structure of the decay $D^0 \to K^0_S K\pi$ was compared to the decay $D^0 \to K^0_S\pi\pi$. I am reporting an absolute branching ratio for the decay $D^0 \to K^{*+}K^-$, where I see a clear signal. For the remaining decay modes (sub-samples), 90% confidence level upper limits are reported. A summary of the final results are listed in Table 5.1.

D^0 decay mode	Relative branching ratio	Absolute branching ratio (%)
$K^{*+}K^-$	$0.21\pm0.04\pm0.03$	$1.1\ \pm0.2\pm0.2\pm0.1$
$K^{*-}K^+$	< 0.07	< 0.37
$\overline{K}^{*0}K^0$	< 0.11	< 0.57
$K^{*0}\overline{K}^0$	< 0.08	< 0.45
$K^0K^-\pi^+$ (non-resonant)	< 0.05	< 0.26
$\overline{K}^0K^+\pi^-$ (non-resonant)	< 0.05	< 0.25

Table 5.1: Relative and absolute branching ratios and 90% confidence level upper limits. Relative branching ratios are calculated by comparing with the decay $D^0 \to K^0_S\pi\pi$. The Particle Data Group branching ratio for the decay $D^0 \to \overline{K}^0\pi^+\pi^-$, $(5.4\pm0.5)\%$, was used to obtain the absolute branching ratios. The errors are statistical and systematic respectively. The third error on the absolute branching ratio of $K^{*+}K^-$ is from the 11% error in the $D^0 \to \overline{K}^0\pi^+\pi^-$ branching ratio.

The systematic errors were computed by varying the Čerenkov efficiency for identifying kaons, the difference between the widths of $K^0_S K\pi$ and $K^0_S \pi\pi$ signals and the relative observation efficiencies ϵ_{ij} calculated from Monte Carlo data. The major contributor to the systematic errors was the relative observation efficiencies ϵ_{ij} calculated from Monte Carlo events. With a better understanding of the Monte Carlo data we should be able to reduce this systematic error to a 10% level. The upper limits reported here do not include any accounting for systematic uncertainties.

Decay mode	Absolute Branching Ratio (%)	
	E791	Others
$K^{*+}K^-$	$1.1 \pm 0.2 \pm 0.2 \pm 0.1$	0.34 ± 0.1[$\star$] $0.69\ ^{+0.32}_{-0.26} \pm 0.14$[†] 0.55[$\circ$] 0.66[$\bullet$]
$K^{*-}K^+$	< 0.37	< 0.30[$\star$] < 0.17[†] 0.20[$\circ$] 0.40[$\bullet$]
$\overline{K}^{*0}K^0$	< 0.57	< 0.15[$\star$] < 0.13[†]
$K^{*0}\overline{K}^0$	< 0.45	< 0.08[$\star$] < 0.22[†]
$K^0K^-\pi^+$ (Non-resonant)	< 0.26	<0.53[†]
$\overline{K}^0K^+\pi^-$ (Non-resonant)	< 0.25	$0.42\ ^{+0.23}_{-0.20} \pm 0.09$[†]

Table 5.2: Comparison of the results to those from other experiments and theoretical models. Upper limits are at 90% confidence level. $\star$ - CLEO collaboration[1], † - E691 collaboration[2], $\circ$ - Theoretical prediction by M. Bauer et al.[3], $\bullet$ - Theoretical prediction by B. Yu. Blok et al.[4].

A comparison of these results to those from other experiments and theoretical models is presented in Table 5.2. It is also interesting to compare these results with similar decay from Cabibbo allowed modes. Such a comparison is given in Table 5.3.

	PP	PV	VP
Cabibbo allowed	$K^-\pi^+$ 3.65 ± 0.21	$K^-\rho^+$ 7.3 ± 1.1	$K^{*-}\pi^+$ 4.5 ± 0.6
Cabibbo suppressed	K^-K^+ 0.41 ± 0.04	K^-K^{*+} $\mathbf{1.1 \pm 0.2 \pm 0.2}$	$K^{*-}K^+$ $\mathbf{< 0.37}$

Table 5.3: Comparison with similar decay from Cabibbo allowed modes. The K^-K^{*+} and $K^{*-}K^+$ branching ratios are from my analysis. All the other branching ratios are from the Particle Data Group book [5].

In the decays $K^-\rho^+$ and K^-K^{*+} the vector boson W^+ decays to a vector particle. In the decays $K^{*-}\pi^+$ and $K^{*-}K^+$ the vector boson W^+ decays to a pseudoscalar. From Table 5.3 it is evident that even in the Cabibbo allowed modes the vector boson $W^\pm$ prefers to decay to a vector particle than to a pseudoscalar. Therefore, we have evidence to support the argument that the quarks arising from the vector boson W^+ tend to materialize more frequently as a vector particle than as a pseudoscalar particle.

Appendix A

Kaon Identification Efficiency

The Čerenkov efficiencies for identifying kaons were studied using the D^+ signal from the decay $D^+ \to K^-\pi^+\pi^+$. In this study, first the D^+ signal was reconstructed using the following cuts:

- SDZ of the D^+ vertex greater than 20,
- DIP of the D^+ with respect to the primary vertex less than $40\mu m$,
- Pion Čerenkov probability of each of the pions greater than 0.7,
- Secondary vertices in the target foils were excluded as were all candidates downstream of the interaction counter, and
- Momentum of the kaons required to lie between 6 GeV and 60 GeV.

Then to study the kaon identification efficiency for a given kaon Čerenkov probability α, the signal was divided into two mutually exclusive samples, one with the kaon Čerenkov probability less than α and another with the kaon Čerenkov probability greater than α. Figure A.1 shows the D^+ mass plots from the decay $D^+ \to K^-\pi^+\pi^+$ for Kaon Čerenkov probability below and above 0.15.

Suppose n_1 be the number of events in the D^+ signal for the kaon Čerenkov probability less than α and n_2 be the corresponding number with the kaon Čerenkov probability greater than α. Then the kaon identification efficiency (K_α) for the kaon Čerenkov probability α could be written as

$$\mathrm{K}_\alpha = \frac{n_2}{(n_1 + n_2)}$$

Since n_1 and n_2 are independent variables we could write the uncertainty of K_α as

$$[\delta(\mathrm{K}_\alpha)]^2 = \left(\frac{\partial \mathrm{K}_\alpha}{\partial n_1}\right)^2 \delta n_1^2 + \left(\frac{\partial \mathrm{K}_\alpha}{\partial n_2}\right)^2 \delta n_1^2 \qquad \text{(A.1)}$$

where $\delta\mathrm{K}_\alpha$ = Uncertainty of K_α, δn_1 = Uncertainty of n_1, and

δn_2 = Uncertainty of n_2

After evaluating the derivatives in the expression A.1, $\delta\mathrm{K}_\alpha$ can be written as

$$\delta(\mathrm{K}_\alpha) = \left\{ \left[\frac{n_2}{(n_1 + n_2)^2}\right]^2 \delta n_1^2 + \left[\frac{n_1}{(n_1 + n_2)^2}\right]^2 \delta n_2^2 \right\}^{\frac{1}{2}}$$

Kaon identification efficiencies for different values of the kaon Čerenkov probability are listed in Table A.1.

Kaon Čerenkov probability	Kaon Identification efficiency
0.11	0.92 ± 0.01
0.13	0.76 ± 0.02
0.15	0.75 ± 0.02
0.20	0.71 ± 0.02
0.30	0.65 ± 0.02
0.40	0.61 ± 0.02

Table A.1: Kaon identification efficiencies as a function of kaon Čerenkov probability for kaon momentum between 6 and 60 GeV.

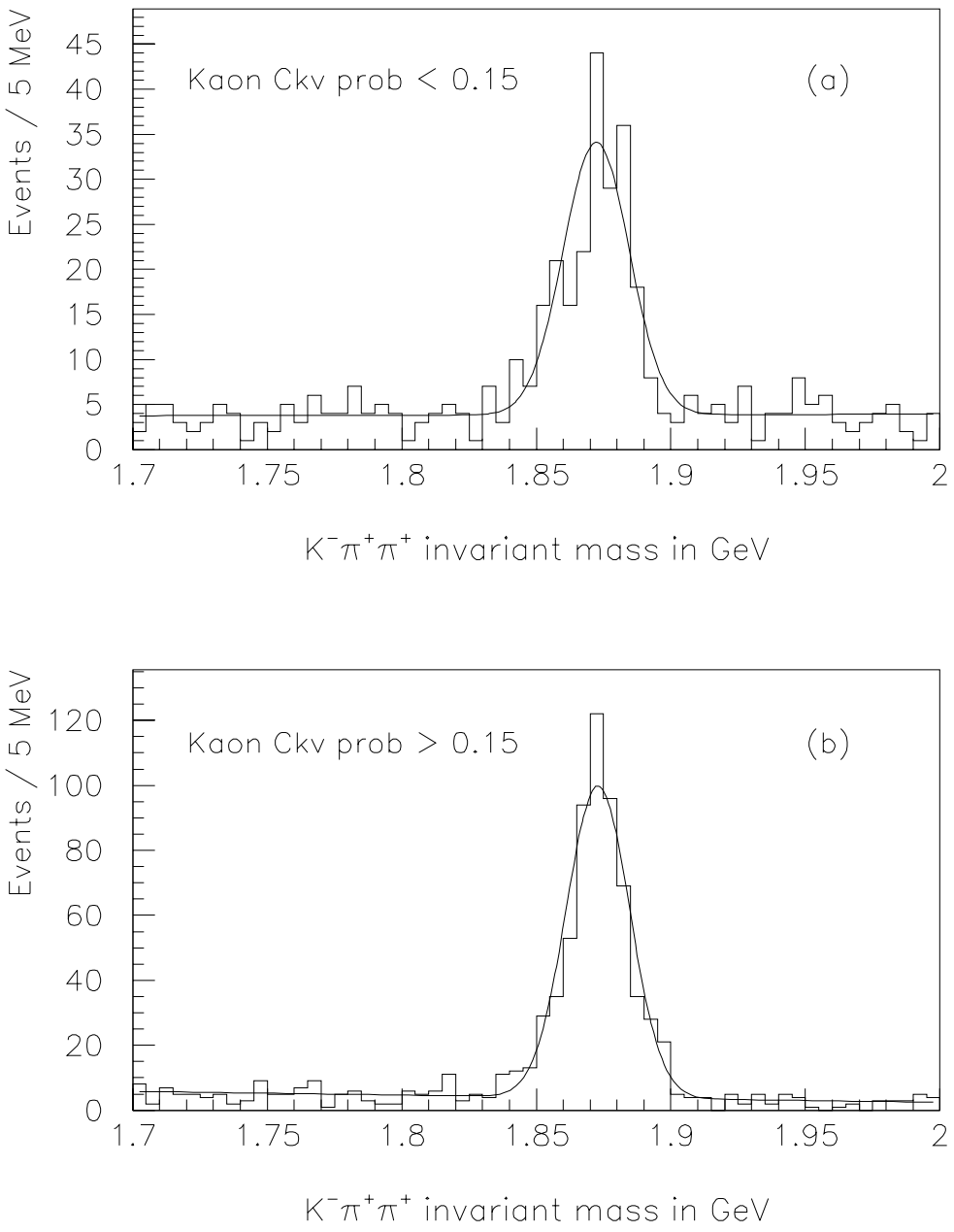

Figure A.1: D^+ mass plots from the decay $D^+ \rightarrow K^-\pi^+\pi^+$ for kaon momentum between 6 and 60 GeV. **(a)** Kaon Čerenkov probability less than 0.15 **(b)** Kaon Čerenkov probability greater than than 0.15

Appendix B

Efficiency Matrix ϵ_{ij}

In the analysis presented in this thesis, I am comparing the sub-structure of the decay $D^0 \to K^0_S K\pi$ with the decay $D^0 \to K^0_S \pi\pi$. These two decays have different sub structures, and the different $D^0 \to K^0_S K\pi$ decay channels ($K^{*+}K^-$, $\overline{K}^{*0}K^0$ and non-resonant $K^0_S K^-\pi^+$) populate different regions of the phase space. Additionally, only 67% of the K^* decays will produce charged pions; the rest will produce neutral pions. We also use the Čerenkov information, which has its own efficiencies to identify kaons in selecting the $D^0 \to K^0_S K\pi$ candidates. To compare the different decays, we have to correct the observed number of events for these efficiencies. I use an efficiency matrix, ϵ_{ij}, in the global maximum likelihood fit to make these corrections. It gives the relative observation efficiency for the $D^0 \to K^0_S K\pi$ decays with respect to $D^0 \to K^0_S \pi\pi$. First I will discuss relative efficiencies for observing the resonant and non-resonant components of the decay $D^0 \to K^0_S K\pi$. Then I will discuss the efficiency for detecting $D^0 \to K^0_S K\pi$ signal relative to that for detecting $D^0 \to K^0_S \pi\pi$ signal.

B.1 Relative Observation Efficiencies Among the Sub-Structure of the Decay $D^0 \to K^0_S K\pi$

In my analysis, the candidate events for the decay $D^0 \to K^0_S K\pi$ were first divided into three sub-samples according to the apparent sub-structure of the decays, $K^{*+}K^-$ or $K^{*-}K^+$, $\overline{K}^{*0}K^0$ or $\overline{K}^{*0}K^0$ and non-resonant $K^0_S K^+\pi^-$ or $K^0_S K^-\pi^+$, in that order. Due to the cuts used to define the sub-samples and the selection order, which are explained in section 4.2, not all the events produces as a given decay will be observed as that decay. For example, a real $K^{*+}K^-$ decay might be observed as $\overline{K}^{*0}K^0$ (unlikely) or as non-resonant $K^0_S K^-\pi^+$ (more likely) decays. I use the efficiency coefficients ϵ_{ij} to describe this process quantitatively.

I have calculated the values of the efficiency coefficients ϵ_{ij} using Monte Carlo events. I assume that the efficiency coefficients for the decays $D^0 \to K^0_S K^+\pi^-$ and $D^0 \to K^0_S K^-\pi^+$ as well as for the charge conjugate modes are identical. First, I generated Monte Carlo event samples with the resonant decays $K^{*+}K^-$, $\overline{K}^{*0}K^0$ and the non-resonant decay $K^0_S K^-\pi^+$. Then each Monte Carlo event sample was analyzed identically to data. Figures B.1, B.2 and B.3 show the D^0 mass histograms for the observed events from each of the Monte Carlo event samples. Histograms in these figures were fitted with a gaussian signal and a linear background. A summary of the number of observed events, n_{ij}, is listed in Table B.1 where n_{ij} is the number of the events from the true decay "j" observed as the decay "i".

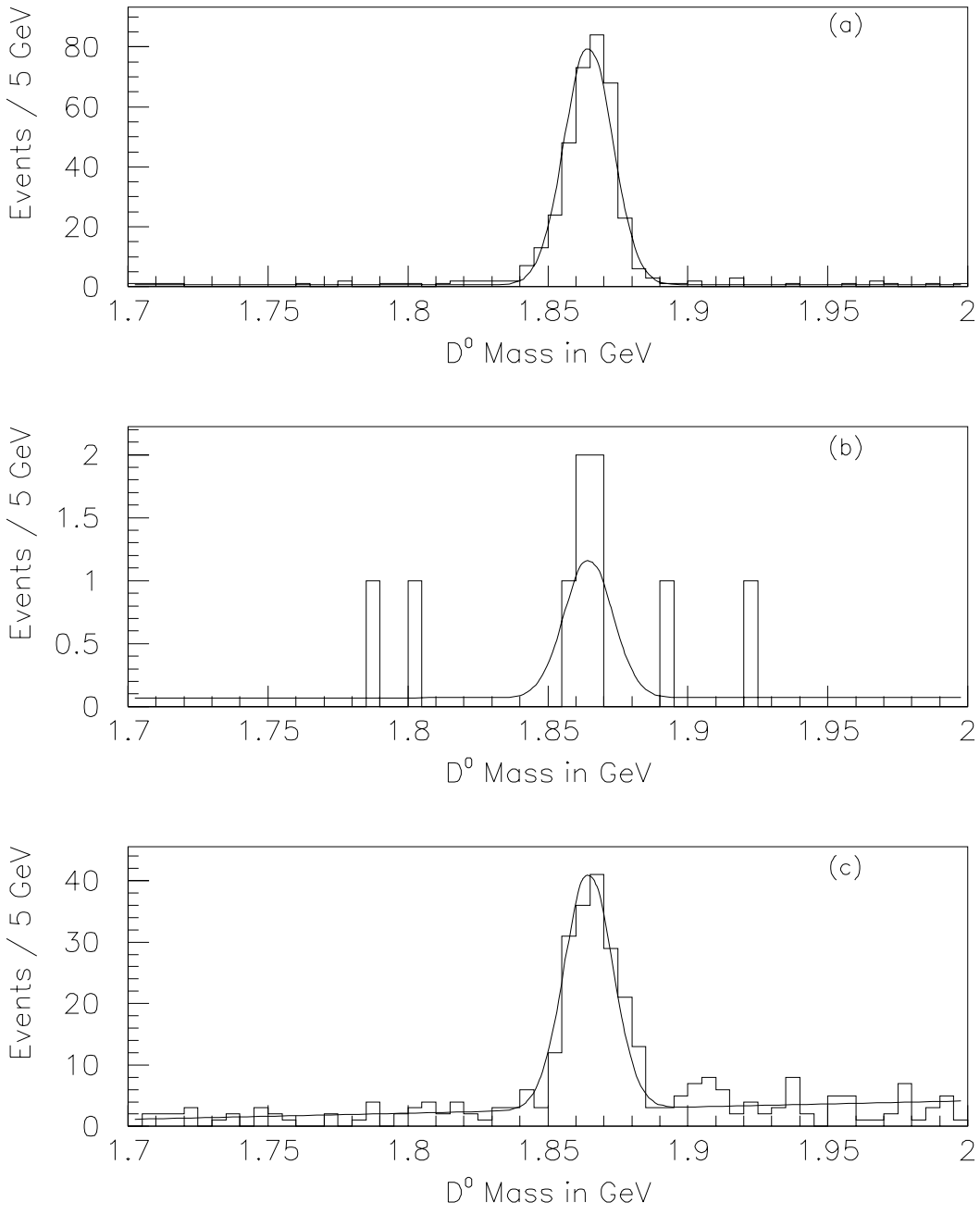

Figure B.1: $K^0_S K^- \pi^+$ invariant mass histograms for the observed events from a $D^0 \rightarrow K^{*+} K^-$ Monte Carlo event sample. (**a**) Observed as $K^{*+} K^-$ (**b**) Observed as $\overline{K}^{*0} K^0$ (**c**) Observed as non-resonant $K^0_S K^- \pi^+$

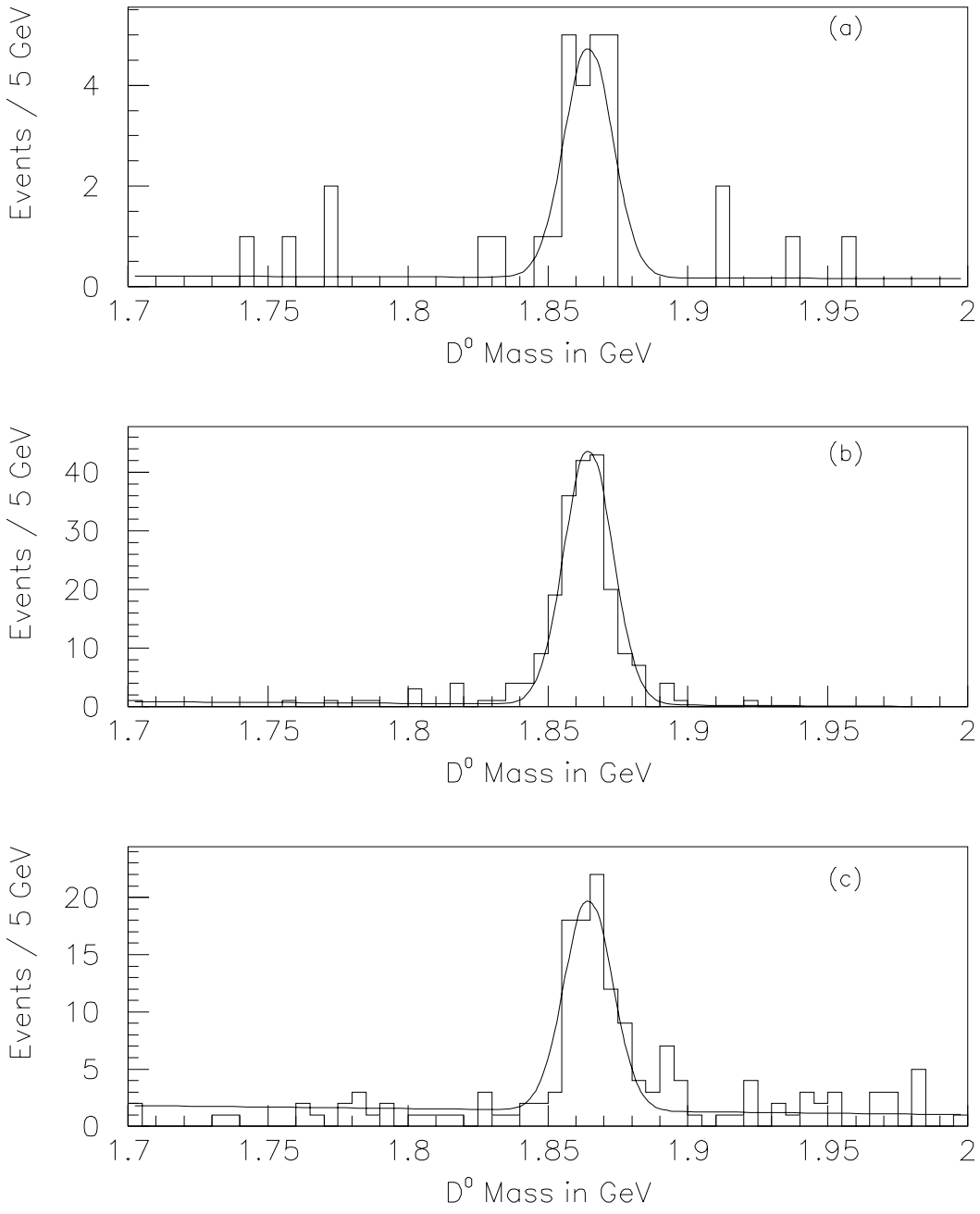

Figure B.2: $K^0_S K^- \pi^+$ invariant mass histograms for the observed events from a $D^0 \to \overline{K}^{*0} K^0$ Monte Carlo event sample. (**a**) Observed as $K^{*+} K^-$. (**b**) Observed as $\overline{K}^{*0} K^0$. (**c**) Observed as non-resonant $K^0_S K^- \pi^+$.

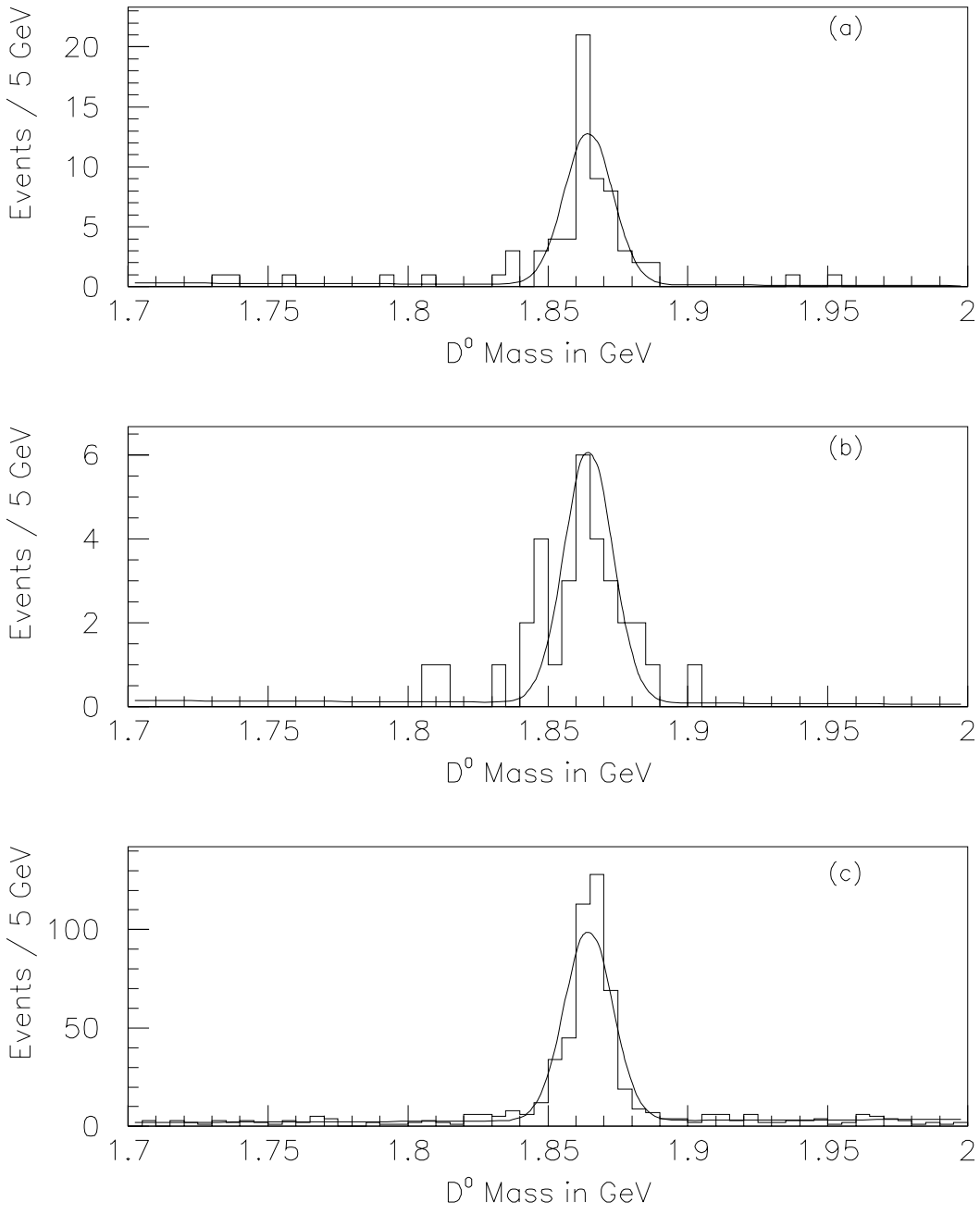

Figure B.3: $K^0_S K^- \pi^+$ invariant mass histograms for the observed events from a non-resonant $D^0 \rightarrow K^0_S K \pi$ Monte Carlo event sample. (**a**) Observed as $K^{*+} K^-$ (**b**) Observed as $\overline{K}^{*0} K^0$ (**c**) Observed as non-resonant $K^0_S K^- \pi^+$

		Produced as		
	n_{ij}	$K^{*+}K^-$	$\overline{K}^{*0}K^0$	Non-resonant
O B S E R V E	$K^{*+}K^-$	343±19	20±5	55±8
	$\overline{K}^{*0}K^-$	5±3	189±14	26±6
	Non-resonant	166±14	80±10	418±21

Table B.1: A summary of the number of observed events in each of the D^0 mass plots in the Figures B.1, B.2 and B.3. Where n_{ij} is the number of the events from the true decay "j" observed as the decay "i"

The observation efficiencies ϵ_{ij} are defined as,

$$\epsilon_{ij} = \frac{n_{ij}}{n_{1j} + n_{2j} + n_{3j}} \qquad \text{where } i,j = 1,2,3 \tag{B.1}$$

The elements of the matrix ϵ_{ij} have the following meanings.

ϵ_{11} :- Fraction of the produced $K^{*+}K^-$ signal observed as the $K^{*+}K^-$

ϵ_{12} :- Fraction of the produced $\overline{K}^{*0}K^0$ signal observed as $K^{*+}K^-$

ϵ_{13} :- Fraction of the produced non-resonant $K^0_S K^-\pi^+$ signal observed as $K^{*+}K^-$

ϵ_{21} :- Fraction of the produced $K^{*+}K^-$ signal observed as $\overline{K}^{*0}K^0$

ϵ_{22} :- Fraction of the produced $\overline{K}^{*0}K^0$ signal observed as $\overline{K}^{*0}K^0$

ϵ_{23} :- Fraction of the produced $\overline{K}^{*0}K^0$ signal observed as non-resonant $K^0_S K^-\pi^+$

ϵ_{31} :- Fraction of the produced non-resonant $K^0_S K^-\pi^+$ signal observed as $K^{*+}K^-$

ϵ_{32} :- Fraction of the produced non-resonant $K^0_S K^-\pi^+$ signal observed as $\overline{K}^{*0}K^0$

ϵ_{33} :- Fraction of the produced non-resonant $K^0_S K^-\pi^+$ signal observed as non-resonant $K^0_S K^-\pi^+$

The values of the efficiency matrix ϵ_{ij} calculated using the formula B.1 are listed in Table B.2. Errors were estimated by taking ϵ_{ij} as a function of three independent variables n_{1j}, n_{2j} and n_{3j}.

		Produced as		
	ϵ_{ij}	$K^{*+}K^-$	$\overline{K}^{*0}K^0$	Non-resonant
OBSERVE	$K^{*+}K^-$	0.67±0.03	0.069±0.005	0.110±0.005
	$\overline{K}^{*0}K^-$	0.010±0.002	0.65±0.04	0.052±0.003
	Non-resonant	0.32±0.01	0.28±0.02	0.84±0.04

Table B.2: Observation efficiencies ϵ_{ij} for the decays $K^{*+}K^-$, $\overline{K}^{*0}K^0$ and non-resonant $K^0_S K^-\pi^+$ calculated using the formula B.1

B.2 Correcting ϵ_{ij} for the Fraction of K^*s Decaying to Charged Pions

Due to the isospin structure of the K^* decays, only 67% of the K^*s produce charged pions; the rest of the K^* decays produce neutral pions. That means, if $K^{*+}K^-$, $\overline{K}^{*0}K^0$, and non-resonant $K^0_S K^+\pi^-$ decays are produced at equal rates, then only 67% of the K^* events will be observed as $K^0_S K^+\pi^-$, compared to the non-resonant $K^0_S K^+\pi^-$ decays, provided all the other observation efficiencies for the K^* and non-resonant decay are equal. To correct for this, the K^* efficiency columns in the matrix ϵ_{ij} must be multiplied by 0.67.

B.3 Correcting ϵ_{ij} for the Čerenkov Efficiency for Identifying Kaons

I require that the Čerenkov probability of the kaons in the $K^0_S K\pi$ candidates be greater than 0.15. From the Čerenkov studies described in appendix A, I have found the efficiency for identifying kaons to be 0.75 ± 0.02 for this Čerenkov probability cut. Therefore, just due to the Čerenkov probability cut, the observation efficiency of $K^0_S K\pi$ candidates is 75% compared to $K^0_S\pi\pi$ candidates. All the elements in the efficiency matrix ϵ_{ij} must be multiplied by 0.75 to get the correct relative efficiency for identifying $K^0_S K\pi$ candidates.

B.4 Correcting ϵ_{ij} for the Relative Reconstruction Efficiency

The decays $D^0 \to K^{*+}K^-$, $D^0 \to \overline{K}^{*0}K^0$, non-resonant $D^0 \to K^0_S K\pi$, and $D^0 \to K^0_S\pi\pi$ may have different reconstruction efficiencies (even excluding the Čerenkov efficiency for identifying kaons, and the K^* mass and angular cuts described in section 4.2). One reason for this difference is the $K\pi/\pi\pi$ vertex reconstruction efficiency which is a function of the opening angle of the two tracks in the $K\pi/\pi\pi$ vertex and the momentum of the $K\pi/\pi\pi$ pair; details of which are given in appendix E.

I measured these relative reconstruction efficiencies using Monte Carlo data. First, I generated Monte Carlo event samples for each of the decays $D^0 \to K^{*+}K^-$, $D^0 \to \overline{K}^{*0}K^0$, non-resonant $D^0 \to K^0_S K\pi$, and $D^0 \to K^0_S\pi\pi$. The $D^0 \to K^0_S\pi\pi$ Monte Carlo events were generated with the correct sub-structure as in the Particle Data Group book[5]. Then, using the Monte Carlo truth table information, the number of correctly

reconstructed D^0 candidates[1], passing the final analysis cuts, was measured. Here, the D^0 candidates were reconstructed identically to the analysis, except the Čerenkov information for identifying kaons and K^* selection cuts described in section 4.2 were not used. The ratio of the number of correctly reconstructed D^0 candidates to that of the total D^0 candidates in the Monte Carlo sample which were within the acceptance of the spectrometer was taken as the absolute reconstruction efficiency. The absolute reconstruction efficiencies were then divided by that of the $D^0 \to K^0_S\pi\pi$ decay mode to get the relative reconstruction efficiencies. The results of this study are listed in Table B.3.

	Decay Mode			
	$K^{*+}K^-$	$\overline{K}^{*0}K^0$	non-resonant $K^0_SK\pi$	$K^0_S\pi\pi$
Amount within acceptance of the spectrometer (%)	64.8±0.4	63.3±0.4	64.0±0.4	63.7±0.3
Absolute reconstruction efficiency *[excluding Čerenkov efficiency and K^* cuts]* (%)	1.00±0.04	0.65±0.03	1.04±0.04	1.26±0.04
Relative reconstruction efficiency	0.79±0.04	0.52±0.03	0.83±0.04	1

Table B.3: Reconstruction efficiency (excluding the Čerenkov efficiency for identifying kaons and K^* mass and angular cuts described in section 4.2). Its defined as the fraction of the correctly reconstructed $D^0 \to K^0_SK\pi$ or $D^0 \to K^0_S\pi\pi$ candidates from the total D^0s in the Monte Carlo sample which were within the acceptance of the spectrometer.

Each column in the efficiency matrix ϵ_{ij} must be multiplied by the corresponding relative reconstruction efficiency from Table B.3 to correct for the differences in the reconstruction efficiencies. Since we use only the relative reconstruction efficiencies, errors in the Monte Carlo simulations which are common to the decay modes being

[1]all the tracks in the D^0 candidate coming from a real D^0 decay

studied here (such as drift chamber efficiencies) should cancel.

B.5 The Final Efficiency Matrix ϵ_{ij}

Table B.4 shows the final relative observation efficiencies for the $D^0 \to K^0_S K\pi$ decay modes with respect to the decay $D^0 \to K^0_S \pi\pi$, obtained as explained earlier in this appendix. The total relative observation efficiency of each of the three decay modes, $K^{*+}K^-$, $\overline{K}^{*0}K^0$, and non-resonant $K^0_S K^-\pi^+$, with respect to the decay $D^0 \to K^0_S\pi\pi$ are listed at the bottom of the Table B.4.

		Produced as		
	ϵ_{ij}	$K^{*+}K^-$	$\overline{K}^{*0}K^0$	Non-resonant
O				
B	$K^{*+}K^-$	0.27±0.02	0.018±0.002	0.068±0.005
S				
E	$\overline{K}^{*0}K^-$	0.0039±0.0008	0.17±0.02	0.032±0.003
R				
V	Non-resonant	0.128±0.008	0.072±0.008	0.52±0.04
E				
D	Total	0.40±0.02	0.26±0.02	0.62±0.04

Table B.4: The final relative observation efficiencies ϵ_{ij} for the decays $K^{*+}K^-$, $\overline{K}^{*0}K^0$, and non-resonant $K^0_S K^-\pi^+$ with respect to the decay $D^0 \to K^0_S\pi\pi$

The total $K^{*+}K^-$ efficiency is lower than the total non-resonant $K^0_S K\pi$ efficiency primarily due to the fraction of K^*s decaying to neutral pions. The total $\overline{K}^{*0}K^0$ efficiency is lower than the $K^{*+}K^-$ total efficiency, because it populates a region of phase space (the Dalitz plot) where the $K\pi$ vertex reconstruction efficiency is lower (see appendix E).

Appendix C

Widths and Reflections

In my analysis I use the following formula to relate the σ of the gaussian signal from the $K^0_S K\pi$ candidates to that from $K^0_S\pi\pi$ candidates (see Appendix C.1).

$$\sigma_{K^0_S K\pi} = \sigma_{K^0_S\pi\pi} - 1.1\,\mathrm{MeV}$$

Also, to exclude the reflection of the $K^0_S\pi\pi$ signal in the $K^0_S K\pi$ invariant mass plots I use only the events in the mass range 1.7 GeV to 1.95 GeV for the $K^0_S K\pi$ sub-samples. Each of these are explained in this appendix.

C.1 Widths of $K^0_S K\pi$ and $K^0_S\pi\pi$ Signals

Figures C.1 and C.2 show the $K^0_S K\pi$ and $K^0_S\pi\pi$ invariant mass histograms from Monte Carlo data. Each of the histograms are fitted separately with a gaussian signal and a linear background. From the fits I find the σ of the $K^0_S K\pi$ signal as 8.4 ± 0.2 MeV and that of the $K^0_S\pi\pi$ signal as 9.5 ± 0.2 MeV.

From histograms in Figures C.1 and C.2 I obtained the difference of the widths of

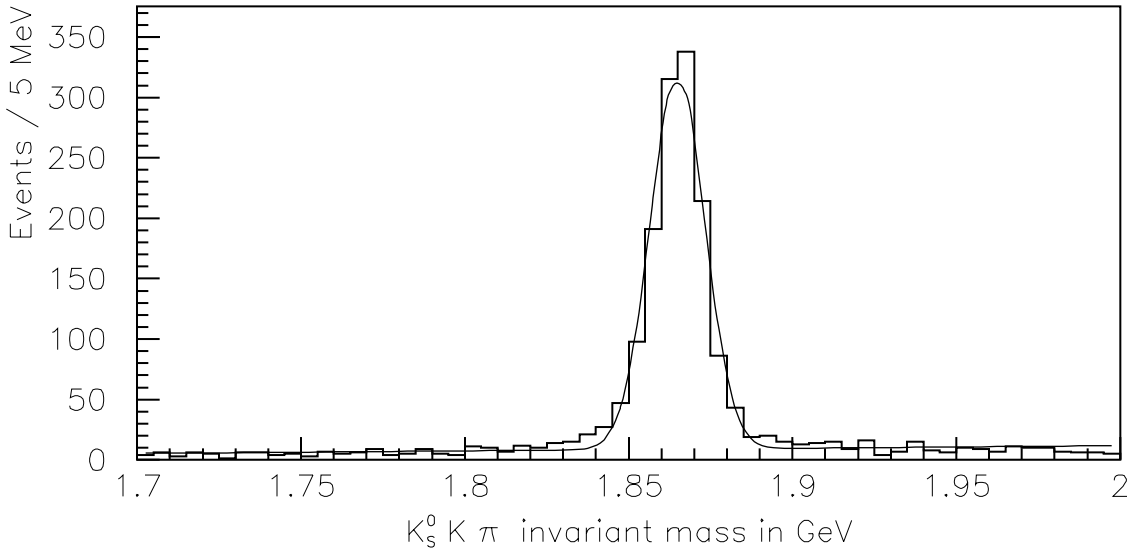

Figure C.1: The $K^0_S K\pi$ invariant mass histogram from the $D^0 \to K^0_S K\pi$ Monte Carlo events. The signal is fitted with a gaussian signal and a linear background. From the fit I find the σ of the signal to be 8.4 ± 0.2 MeV.

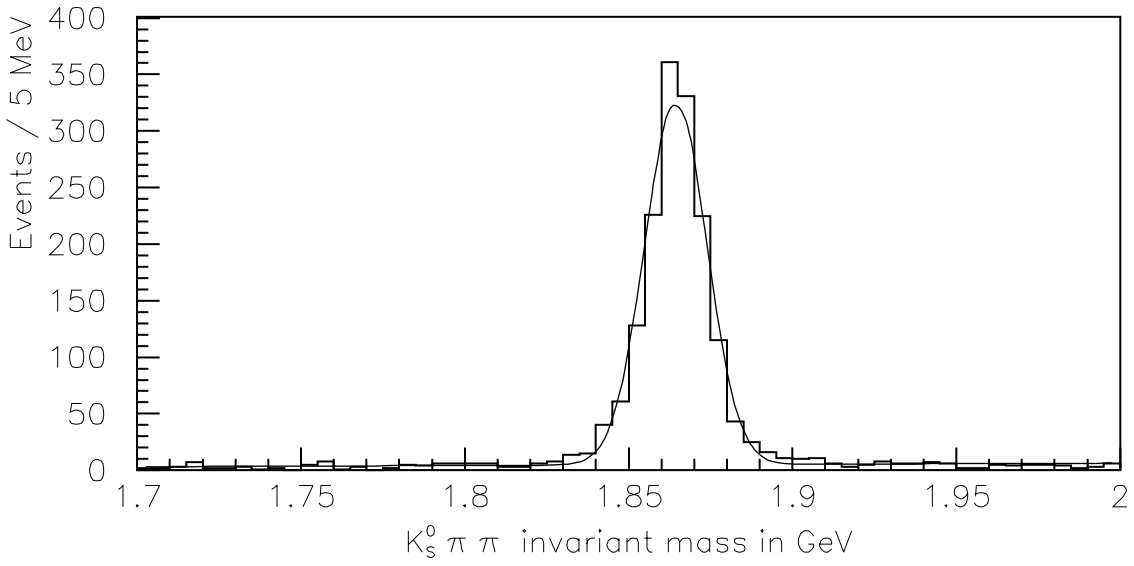

Figure C.2: The $K^0_S \pi\pi$ invariant mass histogram from the $D^0 \to K^0_S \pi\pi$ Monte Carlo events. The signal is fitted with a gaussian signal and a linear background. From the fit I find the σ of the signal to be 9.5 ± 0.2 MeV.

the two signals as 1.1 ± 0.3 MeV. Since the decay $D^0 \to K^0_S K\pi$ has a small Q value[1] compared to the decay $D^0 \to K^0_S \pi\pi$, this difference in widths of the D^0 mass plots is expected. In the analysis, I assume that the same relationship between the widths of $K^0_S K\pi$ and $K^0_S \pi\pi$ signals remains the same in Monte Carlo and data.

[1]The difference between mass of the parent particle and that of all the constituents in the decay.

C.2 Reflection of the $K^0_S\pi\pi$ Signal in the $K^0_SK\pi$ Invariant Mass Plot

Due to the Čerenkov inefficiencies, some real pions are misidentified as kaons. Therefore we could get a systematic reflection of the $K^0_S\pi\pi$ signal in the $K^0_SK\pi$ mass plot. In Figure C.3 I have plotted the $K^0_SK\pi$ invariant mass of the $K^0_S\pi\pi$ signal from Monte Carlo data for events that are also consistent with coming from the decay $D^0 \to K^0_SK\pi$. Since I have not fully understood the modeling of this reflection, in the maximum likelihood fit I use only the events in the mass range 1.7 GeV to 1.95 GeV for the $K^0_SK\pi$ sub-samples.

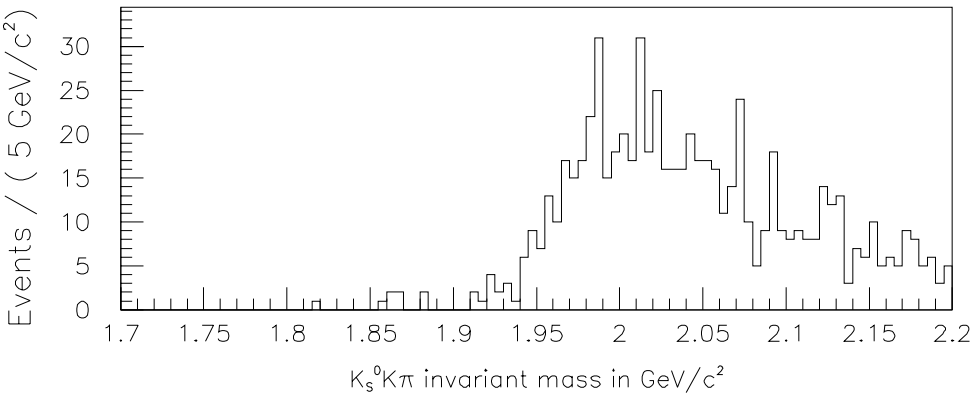

Figure C.3: Reflection of the $K^0_S\pi\pi$ signal in the $K^0_SK\pi$ invariant mass plot. Here I have plotted the $K^0_SK\pi$ invariant mass from the $K^0_S\pi\pi$ Monte Carlo events that are also consistent with coming from the decay $D^0 \to K^0_SK\pi$

Appendix D

The Candidate Driven Search for $K\pi/\pi\pi$ Vertices

The vertex reconstruction algorithm used in E791 was only 16% efficient in reconstructing $K\pi/\pi\pi$ vertices (see section 2.4). To cope with this inefficiency, I used a candidate driven algorithm to reconstruct additional two prong $K\pi/\pi\pi$ vertices.

Due to the short decay length of the D^0 candidates, only the SESTR tracks were used to form two prong vertices in this search. Reconstructed vertices were required to have a minimum SDZ of 6. Most of the two prong vertices reconstructed entirely from tracks that were in the primary vertex failed to pass the above SDZ requirement. Therefore, to save computing time, at most only one track in the reconstructed two prong vertex was allowed to belong to the already reconstructed primary vertex. Additionally, only the category 3, 7, and 15 tracks with a χ^2/ν of five or less were used.

Table D.1 shows the locations of tracks that were supposed to be in the $K\pi$ vertex. I used a $D^0 \to K^0_S K\pi$ Monte Carlo to obtain these numbers.

Location	Percentage(%)
Exactly one of the tracks in the reconstructed primary vertex	33
Both the tracks in the reconstructed primary vertex	27
None of the two tracks in the reconstructed primary vertex	40
Appears as a two prong vertex in the vertex list	16

Table D.1: Locations of the tracks that were supposed to be in the $K\pi$ vertex.

In this search, all the oppositely charged pairs of SESTR tracks passing the above track quality cuts were considered potential candidates for two prong vertices. Also, the necessary precautions were taken to avoid re-reconstruction of the two prong vertices in the *vertex list*. First, the approximate vertex position was calculated and the distance of closest approach of the two tracks used to form the vertex was required to be less than 100 μm. Then the tracks in the vertex was fitted with a χ^2 minimization routine to calculate the position more accurately and to get its error. Primary vertices were not re-fitted. The two prong vertices with the SDZ greater than 6 were kept.

Appendix E

Vertex Reconstruction Efficiency and the Opening Angle Distributions

I studied the dependence of $K\pi/\pi\pi$ vertex reconstruction efficiency on the opening angle of the $K\pi/\pi\pi$ pairs; for this study, I used Monte Carlo data from the decays $D^0 \to K^{*+}K^-$, $D^0 \to \overline{K}^{*0}K^0$, non-resonant $D^0 \to K^0_S K^-\pi^+$, and $D^0 \to K^0_S\pi^+\pi^-$. The $D^0 \to K^0_S\pi^+\pi^-$ Monte Carlo events used in this study were generated with the resonant sub-structure as in the Particle Data Group book [5].

Figure E.1 shows the $K\pi/\pi\pi$ opening angle histograms for these decays. The histograms on the left are for $K\pi/\pi\pi$ pair momenta less than 50 GeV, and the ones on the right are for $K\pi/\pi\pi$ pair momenta greater than 50 GeV. At lower momenta, the opening angle are typically larger; the opening angle distributions more clearly depend on the particular decay modes. For $D^0 \to$ vector + pseudoscalar decays, the opening angle distribution of the $K\pi/\pi\pi$ pair depends on whether the two tracks come from the vector resonance or whether one comes from the resonance and the other is the

pseudoscalar. I explicitly checked the Dalitz plot distributions of each Monte Carlo sample and it's projections to make sure the Monte Carlo generator was producing the correct angular and Breit-Wigner distributions for the decays with vector daughters. The opening angle distributions observed in Figures E.1 and E.2 reflect these phase space and resonant amplitude structures. The opening angle distributions of $D^0 \to K^{*+}K^-$ and $D^0 \to K^0_S\pi^+\pi^-$ decays have a similar structure. This is because most (56% [5]) of the $K^0_S\pi\pi$ events are from the decay $D^0 \to K^{*-}\pi^+$, in which the $K\pi/\pi\pi$ vertex has one track from the resonance and the other is the pseudoscalar.

Figure E.2 shows the $K\pi/\pi\pi$ opening angle distributions for all momenta. The full histograms in Figure E.2 are from the generated $K\pi/\pi\pi$ pairs which were within the acceptance of the spectrometer; the shaded histograms are from the $K\pi/\pi\pi$ pairs reconstructed as two prong vertices in the vertex list with SDZ > 13. The histograms in Figure E.3 show the vertex reconstruction efficiency as a function of the opening angle.

In all decay modes studied here, the vertex reconstruction efficiency falls off at low opening angles of $K\pi/\pi\pi$ pairs. At low opening angles, the error of the reconstructed vertex position becomes larger, making SDZ (see section 3.1.2) of the vertex smaller. Since we require SDZ of the $K\pi/\pi\pi$ vertices be above a minimum value, we expect the vertex detection efficiency to be lower at low opening angles. In the $D^0 \to \overline{K}^{*0}K^0$ decays, both tracks in the $K\pi$ vertex come from the K^*, which has a relatively low mass. Therefore, we observe that the $K\pi$ opening angle here tends to be lower than that from $K^{*+}K^-$, non-resonant $K^0_SK^-\pi^+$ and $K^0_S\pi^+\pi^-$ (which is mostly $K^{*-}\pi^+$) decays.

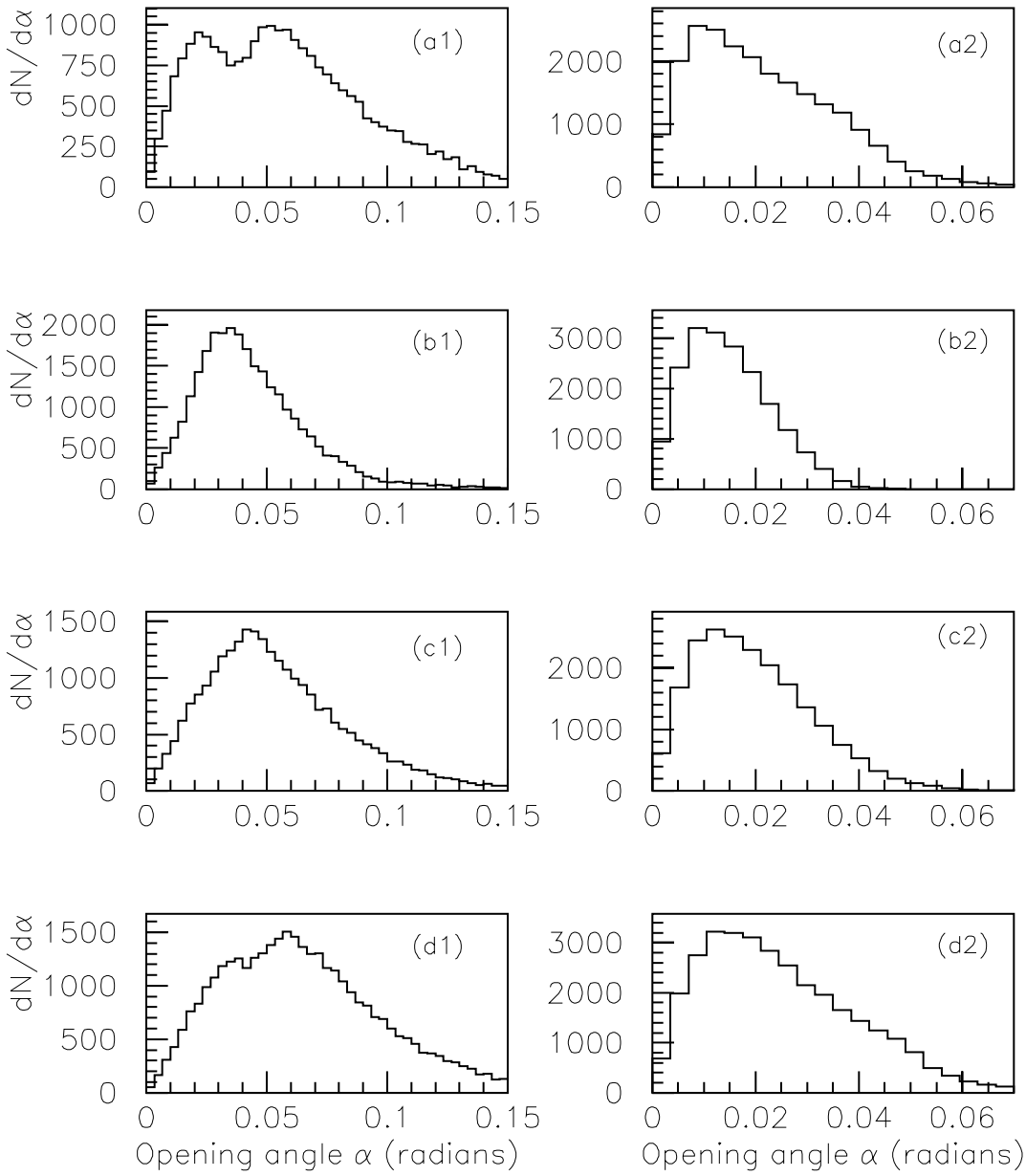

Figure E.1: $K\pi/\pi\pi$ opening angle distributions. The histograms on the left are for $K\pi/\pi\pi$ pair momenta less than 50 GeV, and the ones on the right are for $K\pi/\pi\pi$ pair momenta greater than 50 GeV. **(a1)** and **(a2)** from the decay $D^0 \to K^{*+}K^-$, **(b1)** and **(b2)** from the decay $D^0 \to \overline{K}^{*0}K^0$, **(c1)** and **(c2)** from the non-resonant decay $D^0 \to K^0_S K^-\pi^+$, and **(d1)** and **(d2)** from the decay $D^0 \to K^0_S\pi^+\pi^-$.

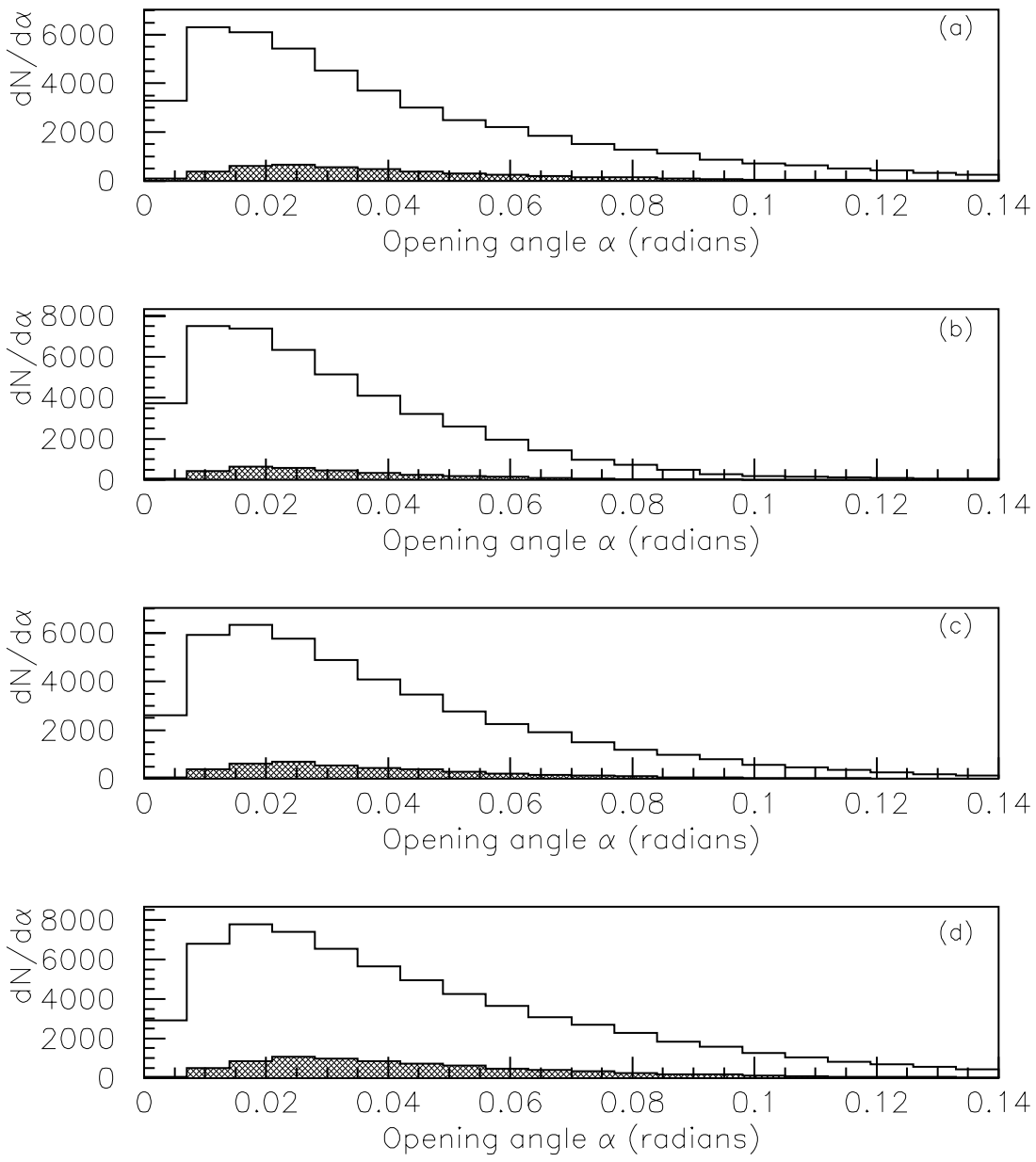

Figure E.2: $K\pi/\pi\pi$ opening angle distributions for all momenta. The full histograms are from the generated $K\pi/\pi\pi$ pairs which were within the acceptance of the spectrometer. The shaded histograms are from the $K\pi/\pi\pi$ pairs that were reconstructed as two prong vertices in the vertex list with SDZ > 13. **(a)** from the decay $D^0 \to K^{*+}K^-$, **(b)** from the decay $D^0 \to \overline{K}^{*0}K^0$, **(c)** from the non-resonant decay $D^0 \to K^0_S K^-\pi^+$, and **(d)** from the decay $D^0 \to K^0_S\pi^+\pi^-$.

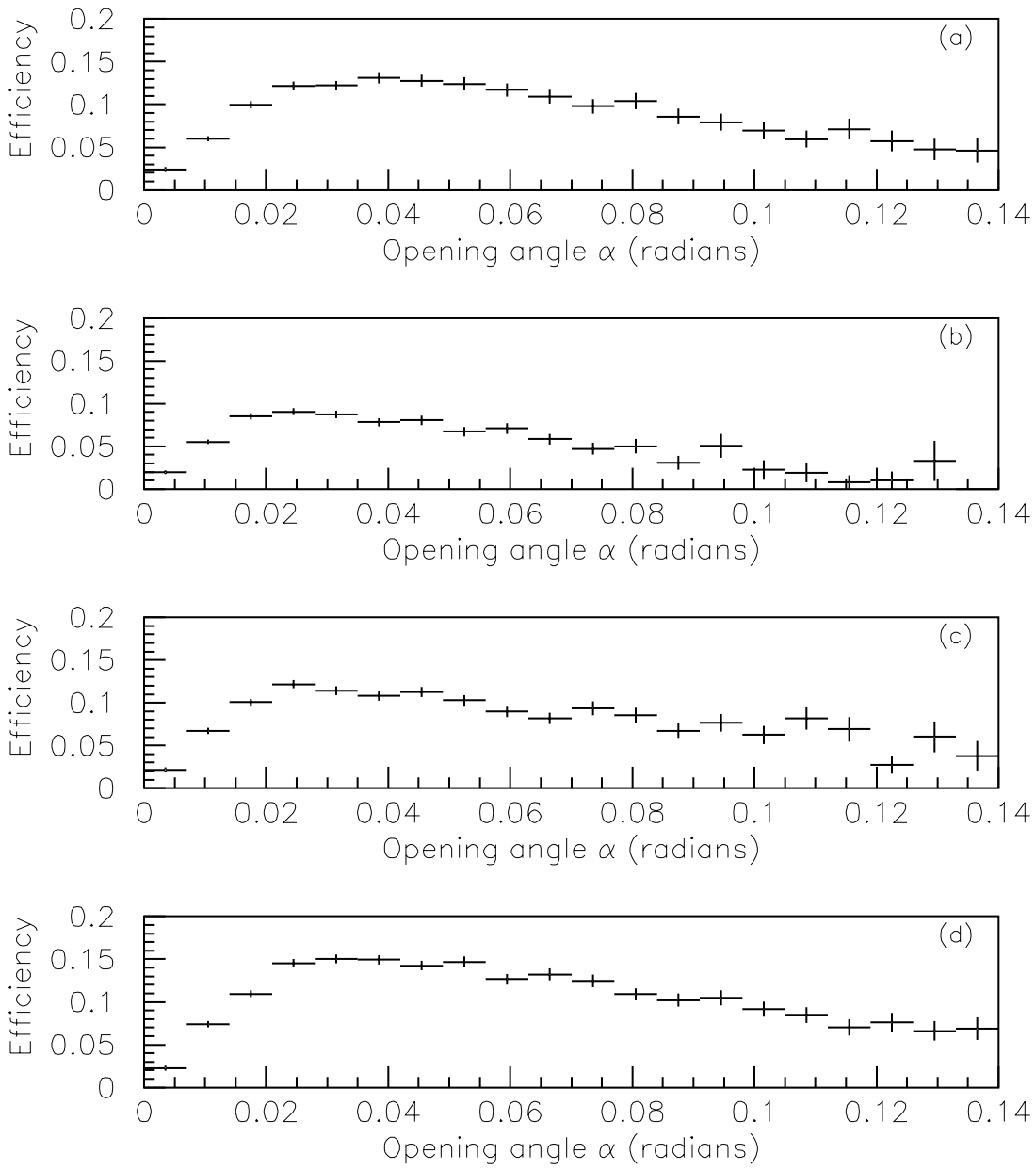

Figure E.3: The fraction of the $K\pi/\pi\pi$ pairs that were within the acceptance of the spectrometer, reconstructed as two prong vertices in the vertex list with SDZ > 13. **(a)** from the decay $D^0 \to K^{*+}K^-$, **(b)** from the decay $D^0 \to \overline{K}^{*0}K^0$, **(c)** from the non-resonant decay $D^0 \to K^0_S K^-\pi^+$, and **(d)** from the decay $D^0 \to K^0_S\pi^+\pi^-$.

Appendix F

90% Confidence Level Upper Limits

When the number of events in the signal region[1] (signal + background) was greater than about 8, I used the gaussian errors to calculate the 90% confidence level upper limits of the signals. Otherwise, I used the Poisson distribution technique described in this appendix.

F.1 Gaussian Errors

The histograms in Figures 4.10 and 4.11, which correspond to non-resonant $K^0_S K^- \pi^+$ and $K^0_S K^+ \pi^-$ decays have more than 10 events (signal + background) in the signal regions. Therefore, I multiplied the gaussian errors from the maximum likelihood fit by 1.28 to get the 90% confidence level upper limits for those signals. Reference [5], section 2.4.1 (page III.38), explains this algorithm.

[1] I used a $\pm 3\sigma$ region around the D^0 mass to define the signal region.

F.2 Poisson Distribution Technique

The $K^0_S K\pi$ invariant mass histograms in Figures 4.5, 4.7, and 4.8, which correspond to the decays $K^{*-}K^+$, $\overline{K}^{*0}K^0$ and $K^{*0}\overline{K}^0$ respectively, have only about one event each in the signal regions. I assumed that the events in these histograms belong to a Poisson process with two components, signal and background. From the maximum likelihood fit, I obtained the predicted number of background events in the signal regions of these histograms. Then, I used the technique described in reference [16] and in section 2.4.4 (page III.40) of reference [5] to calculate the 90% confidence level upper limits for the signals in these histograms.

In this technique, the 90% confidence level upper limits of signals are considered functions of the predicted background in the signal region and the number of observed events in the same region. References [16] and [5] show the curves relating the predicted number of background events in the signal region and the 90% confidence level upper limits of signals, for different number of observed events in the signal region. The 90% confidence level upper limits of the signals in the histograms in Figures 4.5, 4.7, and 4.8, obtained using these curves, are shown in Table F.1.

Decay Mode	Events observed in the signal region	Predicted background events in the signal region	90% confidence level upper limit of signal events
$K^{*-}K^+$ Figure 4.5	1	3±0.5	3±0.5
$\overline{K}^{*0}K^0$ Figure 4.7	1	3±0.5	3±0.5
$K^{*0}\overline{K}^0$ Figure 4.8	0	3±0.5	2.3±0.5

Table F.1: Events observed in the signal region, predicted background in the signal region and the 90% confidence level upper limits for the signals in the histograms in Figures 4.5, 4.7 and 4.8. The errors in the 90% confidence level upper limits are due to the systematic errors of the predicted background events in the signal region.

I obtained the values of the parameters T_3, T_4, andT_5 (number of observed events corrected for efficiencies, see section 4.3.1) corresponding to the 90% confidence level upper limits, as follows: I set the parameter in question to a fixed value, ran the maximum likelihood fit, and checked the predicted number of signal events in the corresponding histogram; I then repeated the procedure, until the predicted number of signal events in the corresponding histogram matched to the 90% confidence level upper limit value shown in column three of Table F.1.

Bibliography

[1] R. Ammar *et al.,* Unusual decay modes of D^0 and D^+ mesons, *Phys. Rev.* **D44**, 3383 (1991).

[2] J. C. Anjos *et al.,* Some cabibbo-suppressed decays of the D^0 meson, *Phys. Rev.* **D43**, R635 (1991).

[3] M. Bauer, B. Stech, and M. Wirbel, Exclusive non-leptonic decays of D, D_s and B mesons, *Z. Phys.* **C34**, 103 (1987).

[4] B. Yu. Blok and M. A. Shifman, Weak non-leptonic deacys of charmed mesons, comparing theory with experiment, *Sov. J. Nucl. Phys.* **45**, 522 (1987).

[5] L. S. Brown *et al.,* Review of particle properties, *Phys. Rev.* **D45** (1992).

[6] S. L. Glashow, Partial symmetries in weak interactions, *Nucl. Phys.* **22**, 579 (1961).

[7] S. Weinberg, A model of leptons, *Phys. Rev. Lett.* **19**, 1264 (1967).

[8] A. Salam, Weak and electromagnetic interactions, In N. Svartholm, editor, *Elementary Particle Theory, Proceedings of the Eigth Nobel Symposium*, page 376, Almquist and Wiksell, Stockholm (1968).

[9] M. Kobayashi and T. Maskawa, CP violation in the renormalizable theory of weak interactions, *Progress of Theoretical Physics* **49**, 647 (1973).

[10] N. Cabbibo, Unitary symmetry and leptonic decays, *Phys. Rev. Lett.* **10**, 531 (1963).

[11] S. L. Glashow, J. Iliopoulos, and L. Maiani, Weak interactions with lepton-hadron symmetry. *Phys. Rev.* **D2**, 1285 (1970).

[12] D. Bartlett *et al.,* Performance of the Čerenkov counters at the Fermilab Tagged Photon Spectrometer Facility, *Nuclear Instruments and Methods in Physics Research* **A260**, 55 (1987).

[13] J.A. Appel *et al.,* Hadron Calorimetry at the Fermilab Tagged Photon Spectrometer Facility, *Nuclear Instruments and Methods in Physics Research* **A243**, 361 (1986).

[14] Pauline Gagnon, *Measurement of the Form Factors in the Semileptonic Decay* $D^+ \rightarrow \overline{K}^{*0} e^+ \nu_e$, PhD thesis, University of California, Santa Cruz, December 1993.

[15] S. Amato *et al.,* The E791 parallel data acquisition system, *Nuclear Instruments and Methods in Physics Research* **A324**, 535 (1993).

[16] O. Helene, Upper limit of peak area, *Nuclear Instruments and Methods in Physics Research* **212**, 319 (1983).